Journal of Materials Chemistry A

ROYAL SOCIETY OF CHEMISTRY

REVIEW

View Article Online
View Journal | View Issue

Cite this: J. Mater. Chem. A, 2025, 13, 11989

UiO-66 (Zr) metal–organic framework for photocatalytic CO_2 reduction: functional design strategies for sustainable carbon utilization

Yongtao Xue and Jia Wei Chew *

Photocatalytic CO_2 reduction is a promising approach to mitigate environmental problems caused by excessive CO_2 emissions while reducing over-reliance on fossil fuels by converting CO_2 into valuable products. Recently, the UiO-66 (Zr) metal–organic framework has been recognized as an excellent candidate for photocatalytic CO_2 reduction due to its porous structure, large specific surface area, and excellent CO_2 adsorption capacity. Remarkable progress has been made, so it is timely to comprehensively review the state-of-the-art functional design strategies for UiO-66 targeted at photocatalytic CO_2 reduction. In this review, the fundamentals of photocatalytic CO_2 reduction and the advances of UiO-66 are critically summarized. Subsequently, the separation efficiency of photogenerated electrons and holes, recognized as a key parameter affecting photocatalytic CO_2 reduction, is discussed, along with methods for its evaluation. The strategies for systematically designing UiO-66 for improving the efficiency of photocatalytic CO_2 reduction are thoroughly assessed. Finally, the challenges for photocatalytic CO_2 reduction by UiO-66 are presented, and recommendations for future studies are proposed. This review is expected to provide new insights to advance the development of photocatalytic CO_2 reduction using UiO-66 and to inspire innovative approaches for overcoming the current limitations.

Received 15th January 2025
Accepted 25th March 2025

DOI: 10.1039/d5ta00388a

rsc.li/materials-a

1. Introduction

Since the industrial revolution, the escalating energy demands have led to an increasing consumption of fossil fuels (*e.g.*, coal, oil, gas), which has triggered detrimental environmental problems and consequently sprouted urgent clean energy challenges.[1] As one of the most serious issues, excessive CO_2 emissions have attracted considerable attention due to the dire severity of global warming, climate change and glacier melting.[2,3] At present, there are two main strategies to address these issues, namely, developing cleaner or renewable energy to reduce the consumption of fossil fuels (*e.g.*, solar energy), and converting CO_2 into valuable chemicals.[4] Although cleaner and renewable energy has developed rapidly, fossil fuels are foreseeably still the main source of energy in the coming few decades.[5] Therefore, effective and efficient utilization of the inevitable CO_2 emitted to produce valuable fuels or products is needed to alleviate the environmental problems and energy shortage crisis. Hitherto, various methods, such as electrochemical CO_2 reduction,[6] photocatalytic CO_2 reduction,[7] preparation of metal–CO_2 batteries,[8] thermocatalytic hydrogenation,[9] synthesis of carbonate,[10] and CO_2 bioconversion,[11] have been devised for CO_2 utilization. Among them, photocatalytic CO_2 reduction has been recognized as a green and sustainable process for the conversion of CO_2 into valuable products due to the reliance on renewable solar energy.

In a typical photocatalytic CO_2 reduction process, the photocatalyst absorbs light for the generation of electrons and holes, which participate in reduction and oxidation, respectively.[12] Recently, various photocatalysts, such as Er-doped $ZnIn_2S_4$,[13] $CuInP_2S_6$,[14] Co_3O_4/Cu_2O,[15] WO_x/g-C_3N_4,[16] Ni-MOF-74,[17] UiO-66,[18] halide perovskite,[19] have been synthesized and applied for photocatalytic CO_2 reduction. It is well-acknowledged that the ideal photocatalyst for photocatalytic CO_2 reduction should have high CO_2 adsorption capacity, outstanding light harvesting efficiency, abundant active sites, excellent separation efficiency of photogenerated electrons and holes, and low toxicity and high stability.[20] Unfortunately, there is not yet a photocatalyst that can satisfy all the above properties concurrently. Hence, it seems feasible and reasonable to select a suitable catalyst that meets most of the requirements and then modify it for photocatalytic CO_2 reduction.

Among all the reported photocatalysts, UiO-66 (Zr) metal–organic framework (MOF) has received much more attention for photocatalytic CO_2 reduction due to its large specific surface area, advantageous pore structures, high CO_2 adsorption capacity, and tunable band structures.[21] However, the wide bandgap that restricts UV light absorption, as well as recombination of photogenerated electrons and holes of UiO-66

Division of Chemical Engineering, Chalmers University of Technology, Gothenburg 412 96, Sweden. E-mail: jia.chew@chalmers.se

hampers its performance for photocatalytic CO_2 reduction. To address this, several modifications, including metallic doping,[22] defect engineering,[23] and fabrication of heterojunctions,[24] have been reported to enhance the performance of photocatalytic CO_2 reduction. To further improve the efficiency of photocatalytic CO_2 reduction by UiO-66, a detailed and comprehensive review of the current state-of-the-art is timely and imperative, so as to provide critical insights for guiding future studies.

Given the widespread recognition of UiO-66's versatility, several reviews have explored its various applications. One review provided a broad overview of its role in the carbon-neutral energy cycle and environmental remediation, covering hydrogen generation, organic pollutant removal, Cr(VI) reduction, and CO_2 reduction.[25] Others have examined defective UiO-66 for energy and environmental remediation applications,[26] using UiO-66 in synthesizing aromatic compounds and fine chemicals,[27] and the broader role of MOFs in photocatalytic CO_2 reduction.[28] However, a dedicated review focusing on the functional design strategies of UiO-66 for photocatalytic CO_2 reduction, along with a comprehensive discussion of the underlying mechanisms, remains lacking. In the present review, the research trends of photocatalytic CO_2 reduction by UiO-66 are investigated through scientometric analysis, and then the fundamentals and challenges of the photocatalytic CO_2 reduction process are critically discussed. Subsequently, the history and advances of UiO-66, as well as the techniques for the identification of charge transfer pathway, are summarized. Following that, the strategies for improving the performance of photocatalytic CO_2 reduction are investigated in detail. Finally, the challenges in the application of UiO-66 for photocatalytic CO_2 reduction are described and future perspectives are proposed.

2. Scientometric analysis

The Web of Science database was employed for the analysis of published papers on UiO-66 for photocatalytic CO_2 reduction. As shown in Fig. 1a, the number of articles on the topics of UiO-66 and photocatalytic CO_2 reduction has increased rapidly in recent years. More than 4000 articles were published on the topic of photocatalytic CO_2 reduction in 2024, underscoring its status as a promising technology. In addition, as the preeminent MOF material, UiO-66 has also received widespread

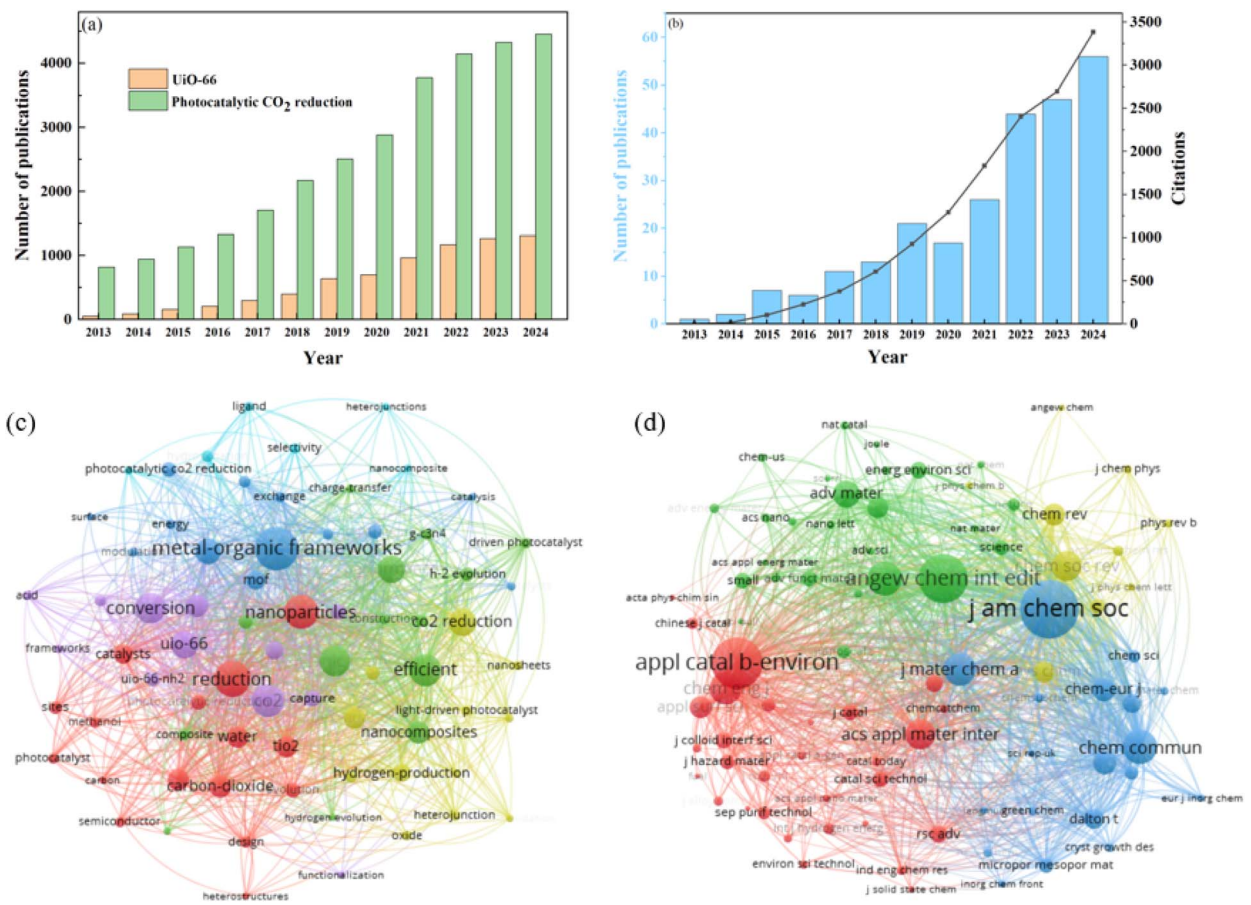

Fig. 1 The number of publications on the topics of UiO-66 and photocatalytic CO_2 reduction (a), the number of publications and citations on the topic of UiO-66 for photocatalytic CO_2 reduction (b). The data were obtained from Web of Science between 2013 and 2024, using advanced search modes (TS 1 = (*UiO-66*); TS 2 = (photo* CO_2 reduction or CO_2 photoreduction or photo* CO_2 conversion or photo* CO_2 utilization or light CO_2 reduction); #TS 1 AND #TS 2). The keywords (c) and co-citation analysis (d) regarding the topic of UiO-66 for photocatalytic CO_2 reduction (#TS 1 AND #TS 2) were obtained using VOSviewer.

attention in the photocatalytic reduction of CO_2. This is evident in Fig. 1b, which shows that the publications and citations on UiO-66 for photocatalytic CO_2 have continuously increased, especially since 2021. Fig. 1c demonstrates that, in addition to keywords UiO-66 and photocatalytic CO_2 reduction (*e.g.*, metal–organic frameworks, carbon dioxide, nanoparticles), efficient, nanocomposites, design, and charge transfer are the main keywords, confirming that the current research focuses on designing UiO-66 catalysts to improve photocatalytic CO_2 performance. The co-citation analysis suggests that this topic is related to chemistry themes through journals like *Journal of the American Chemical Society*, *Angewandte Chemie International Edition*, and material themes through journals like *Advanced Materials*, *Journal of Materials Chemistry A*, as well as environment and energy themes through journals like *Applied Catalysis B-Environment and Energy*, and *Energy & Environmental Science*.

3. Photocatalytic CO_2 reduction: fundamentals and challenges

The photocatalytic CO_2 reduction process is inspired by the photosynthesis of plants, with the first report appearing in 1979 on photocatalytic CO_2 conversion to renewable fuels by semiconductors.[29] In recent years, research dedicated to this topic has developed rapidly, mainly due to considerable focusses on nanomaterial research and advanced technological applications. Theoretically, there are four main steps in photocatalytic CO_2 reduction, namely, (1) adsorption of CO_2 and the reductant, (2) generation of electrons and holes, (3) separation of charge carriers, and (4) reduction of CO_2 and desorption of products.[30]

In the first step of adsorption, it has been reported that the photocatalytic CO_2 reduction process normally occurs on the surface of photocatalysts,[31] hence, the adsorption of CO_2 by photocatalysts as the initiation step is crucial for the reduction. In general, the high CO_2 adsorption capacity of photocatalysts is beneficial for high photocatalytic CO_2 reduction efficiency. For instance, Wang *et al.*[32] confirmed that the outstanding adsorption capacity of Ni_7Co_3–graphene oxide increased the accumulation of CO_2 molecules on the surface, thereby improving the efficiency of photocatalytic CO_2 reduction. Heng *et al.*[33] also observed that the mesoporous structured g-C_3N_4 with a large specific surface area improved CO_2 adsorption capacity, thus resulting in excellent CO_2 conversion efficiency. In addition, it has been reported that there are three main modes of CO_2 adsorption on the surface of photocatalysts, namely, oxygen coordination, carbon coordination, and mixed coordination, which can significantly affect the photocatalytic reduction pathways and final products.[34]

In the second and third steps, the photocatalysts are excited under light irradiation, resulting in the generation of photoelectrons and holes, which are then accumulated in their conduction band and valence band, respectively.[35] Because there is a high possibility of recombination of photoelectrons and holes, the competition between separation and recombination of electrons and holes occurs during the photocatalytic CO_2 reduction process. Therefore, two parameters, namely, light absorption capacity, and separation efficiency of electrons and holes, are key performance indicators. In this regard, various highly efficient visible-light-driven photocatalysts (*e.g.*, α-Fe_2O_3/$LaTiO_2N$,[36] NiAl-LDH/g-C_3N_4,[37] MoS_2 (ref. 38)) have been developed recently, and different strategies (such as fabrication of heterojunction,[39] modification of active sites,[40] construction of defects[41]) have been investigated to improve the separation efficiency of photogenerated electrons and holes during the photocatalytic CO_2 reduction process.

The final step involves the unrecombined electrons and holes participating in further oxidation or reduction reactions to generate the final products. The redox potential for the conversation of CO_2 and H_2O are illustrated in Fig. 2a, indicating that the redox potential of the single-electron pathway for the CO_2 reduction is too high (−1.9 V), mainly due to this value being close to the conduction band edge of most semiconductors.[46] To address this issue, multi-electron reduction pathways (*e.g.*, two electrons, four electrons) are favorable for photocatalytic CO_2 reduction. Since oxidation and reduction occurs simultaneously, hole scavengers are usually applied to consume the holes and improve the separation efficiency of photogenerated electrons and holes, which enhances CO_2 reduction efficiency.[47] Furthermore, a photocatalyst with sufficient negative potential is highly advantageous, indicating requirement for appropriate conduction band and valence band positions. Fortunately, several techniques including non-metallic element doping,[48] metallic element doping,[49] and introduction of oxygen vacancy[50] have been ascertained to be useful for adjusting the conduction band and valence band position of photocatalysts.

In summary, the most important performance-related parameters of photocatalysts include CO_2 adsorption and light absorption capacity, separation efficiency of photogenerated electrons and holes, and conduction band and valence band positions, all of which can greatly affect the CO_2 conversion efficiency during photocatalytic CO_2 reduction.

4. UiO-66: history and advances

UiO-66 ($Zr_6O_4(OH)_4(BDC)_6$), a member of the UiO-MOFs family (stands for University of Oslo), was first synthesized in 2008 by using zirconium oxide ($Zr_6O_4(OH)_4$) as metal nodes and 1,4-benzenedicarboxylic acid (BDC) as the linker.[51] As illustrated in Fig. 2b, the $Zr_6O_4(OH)_4$ octahedron consists of six Zr^{4+} ions, which are connected to four oxygen or hydroxyl groups.[42] Each metal node ($Zr_6O_4(OH)_4$) is coordinated into twelve neighboring metal nodes through BDC links. In addition, the UiO-66 crystal is composed of octahedral cages (12 Å) and tetrahedral cages (7.5 Å), and the pore dimension of triangular cavities is approximately 6 Å.[52] Furthermore, while the theoretical surface area and pore volume of UiO-66 is about 1200 $m^2\ g^{-1}$ and 0.77 $cm^3\ g^{-1}$, respectively, the experimental results indicated specific surface areas of between 500 $m^2\ g^{-1}$ and 1600 $m^2\ g^{-1}$, depending on synthesis routines and structural defects.[53]

Recently, various synthesis methods, including solvothermal, evaporation, and solvent-free, have been developed for the synthesis of UiO-66 with excellent properties. Among

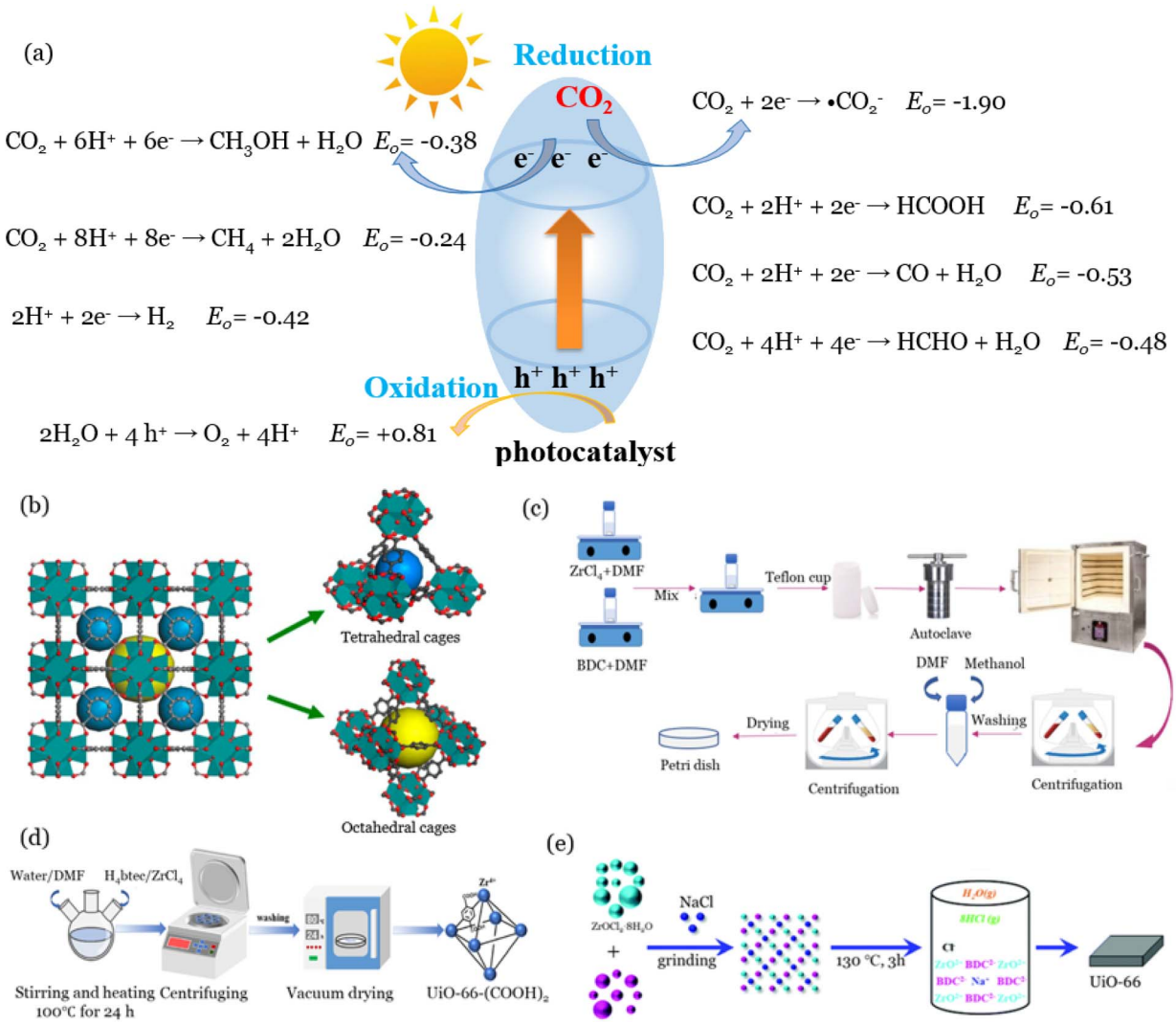

Fig. 2 The redox potential (*vs.* normal hydrogen electrode, pH 7) required for various product formation during the photocatalytic CO_2 reduction process (a); schematic illustration of the UiO-66 (Zr) structure (b), reproduced from ref. 42 with permission from American Chemical Society, copyright 2014. Schematic illustration of various synthesis methods for UiO-66: solvothermal process (c), reproduced from ref. 43 with permission from Springer, copyright 2024. Evaporation (d), reproduced from ref. 44 with permission from Wiley Online Library, copyright 2023. Solvent-free process (e), reproduced from ref. 45 with permission from the Royal Society of Chemistry, copyright 2021.

these methods, the solvothermal process is commonly used, because it allows precise control of the particle size, crystallinity, and morphologies of UiO-66 through the adjustment of synthesis parameters (*e.g.*, reaction temperature and time). In a typical process (Fig. 2c), the $ZrCl_4$ and BDC are well dissolved into dimethylformamide (DMF) solutions under stirring conditions for the formation of a homogenous solution.[43] Subsequently, the obtained solution is transferred into the solvothermal reactor and heated at the temperature of 120 °C for 24 h. After cooling to room temperature, the UiO-66 is washed and dried. Regarding evaporation, it is another simple method for the synthesis of UiO-66 without the requirements of relatively high temperatures and pressures. As an example, Chen *et al.*[44] synthesized the UiO-66-$(COOH)_2$ nanoparticles by using $ZrCl_4$ and 1,2,4,5-benzenetetracarboxylic acid (H_4btec) as the precursor and DMF/water as the reaction solution at a temperature of 100 °C for 24 h (Fig. 2d). As a solvent-free method, Gu *et al.*[45] reported a simple, environmentally friendly, scalable method for the preparation of UiO-66 by using $ZrOCl_2$, BDC, and NaCl as precursors (Fig. 2e). They also observed that NaCl as an additive could promote the diffusion between two precursors and thus improve the crystallization process during the synthesis of UiO-66. Furthermore, some novel and efficient methods, such as fast microwave-assisted method (less than 1 hour)[54] and electrochemical process,[55] have been explored for the preparation of UiO-66.

Although the properties of UiO-66 from different synthesis routines are quite different, most of the prepared UiO-66 typically demonstrates high porosity, large specific surface area, and high UV light absorption, which makes them an excellent candidate for photocatalytic CO_2 reduction. In general, the band gap of pristine UiO-66 is approximately 3.6 eV, which

means that it cannot use visible light for the photoreduction of CO_2.[56] In addition, the fast recombination of photogenerated electrons and holes in UiO-66 restricts their efficiency during photocatalytic CO_2 reduction.[57] To address these issues, several improvement means, including increasing the visible light adsorption capacity and improving the separation efficiency of photogenerated electron pairs, have been developed for UiO-66. The detailed modification process and mechanisms are comprehensively described in the following sections.

5. Identification of charge-transfer pathway

The separation efficiency of photogenerated electrons and holes is one of the most important parameters that can significantly affect the performance of photocatalysts for CO_2 reduction. Therefore, the investigation of charge-transfer pathways is important for effectively improving the separation efficiency of photogenerated electron and hole pairs. In this section, different techniques for evaluating charge-transfer pathways during the photoreduction of CO_2 are discussed, including *in situ* irradiated X-ray photoelectron spectroscopy (ISIXPS), Kelvin probe force microscopy (KPFM), femtosecond transient absorption spectroscopy (fs-TA), electron paramagnetic resonance spectroscopy (EPR), and density functional theory (DFT) calculation.

5.1 *In situ* irradiated X-ray photoelectron spectroscopy (ISIXPS)

X-ray photoelectron spectroscopy (XPS) is a widely used technique for the detection of elemental composition, chemical state, and surface properties of nanomaterials. This technique is very sensitive to the binding energy and chemical environment of the tested materials, with the chemical shift of the element related to the valence state and electron density.[58] The only difference between XPS and ISIXPS is the presence of light irradiation during measurement for the latter. According to the mechanisms of photocatalytic CO_2 reduction, the electron density of the photocatalyst changes under light irradiation due to the movement of photogenerated electrons. Hence, the chemical shifts of the same elements can be compared between dark and light conditions to understand the transfer pathways of photogenerated electrons and holes.[59] For instance, the charge-transfer pathways in the $BiVO_4$/UiO-66-NH_2 (BVO/U6N)

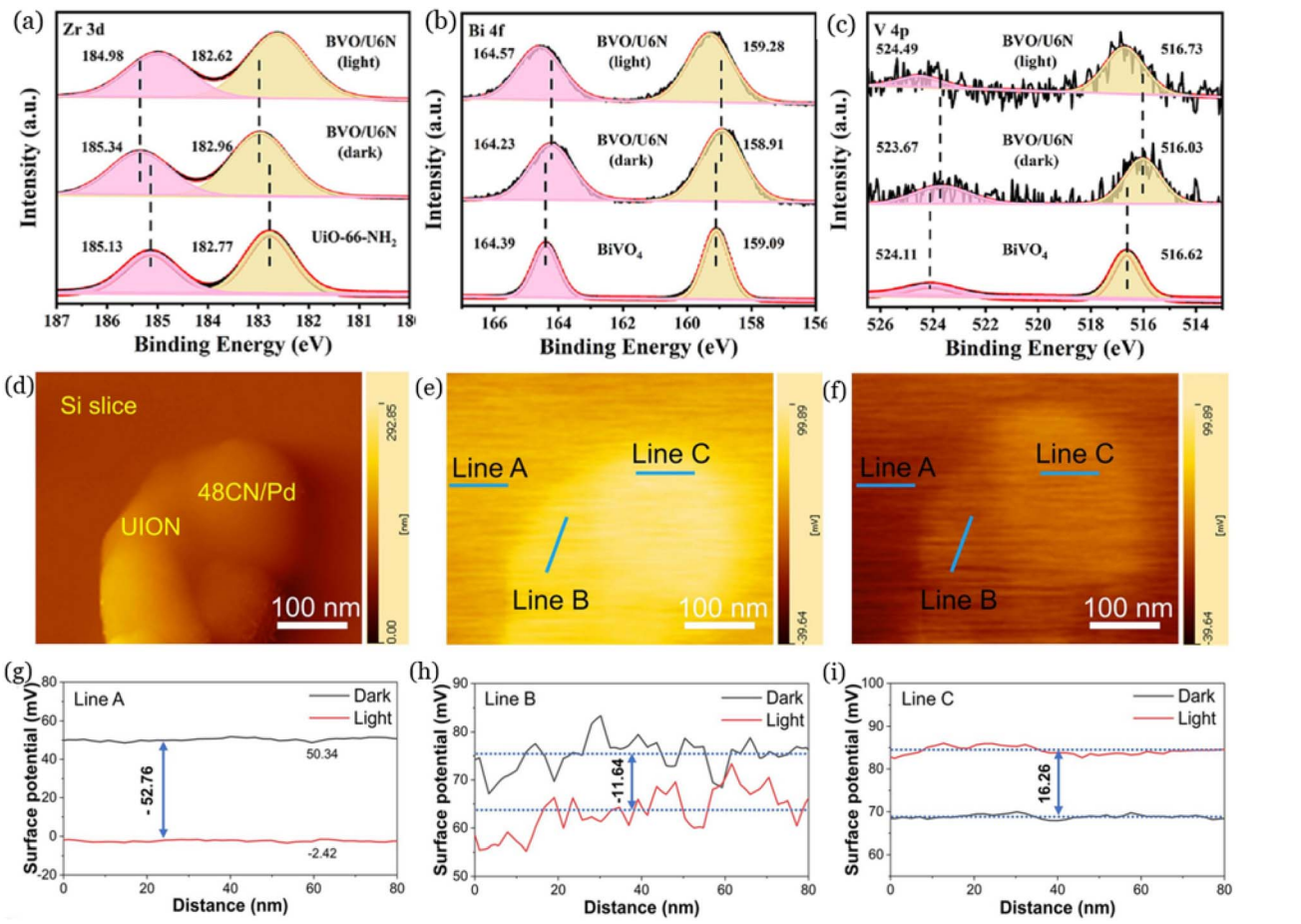

Fig. 3 The ISIXPS spectra of Zr 3d (a), Bi 4f (b), and V 4p (c) of the $BiVO_4$/UiO-66-NH_2 composites, reproduced from ref. 60 with permission from Elsevier, copyright 2023. AFM of UiO-66-NH_2 (UION) and 48CN/Pd (d), KPFM images of 48CN/Pd under dark (e) and light (f) conditions; the surface potentials of line A (g), line B (h), and line C (i), reproduced from ref. 61 with permission from Elsevier, copyright 2023.

composites were investigated through ISIXPS.[60] As illustrated in Fig. 3a, the binding energy of Zr 3d in BVO/U6N shifted to higher energy levels compared to UiO-66-NH_2 under dark conditions, reflecting the decrease of electron density on UiO-66-NH_2. In contrast, the binding energies of Bi 4f and V 4p in BVO/U6N shifted negatively compared to UiO-66-NH_2 under dark conditions (Fig. 3b and c), suggesting the accumulation of electrons on $BiVO_4$ after contact with UiO-66-NH_2. These results are related to the difference in Fermi levels and the formation of an internal electric field due to the strong contact between $BiVO_4$ and UiO-66-NH_2. Under light irradiation, the binding energy of Zr 3d shifted negatively compared to dark conditions, while the binding energies of Bi 4f and V 4p shifted to higher energy levels, indicating that the photogenerated electrons transferred from $BiVO_4$ to UiO-66-NH_2 under light irradiation. Furthermore, this technique has been demonstrated to provide valuable insights for studying the charge transfer pathways and photocatalytic mechanisms of photocatalysts such as MoS_2@-UiO-66-NH_2 (ref. 62) and (Zr/Ce)UiO-66(NH_2)@g-C_3N_4 (ref. 63).

5.2 Kelvin probe force microscopy (KPFM)

Kelvin probe force microscopy (KPFM), which is a derivative of atomic force microscopy (AFM) that can simultaneously detect surface potential and scan surface topography of materials, has been applied for the investigation of photogenerated charge-transfer pathways. In general, when a photocatalyst receives electrons, its Fermi level increases and its surface potential decreases. On the contrary, when a photocatalyst loses electrons, its Fermi level decreases and its surface potential increases.[64] As an example, Liu *et al.*[61] discussed the charge-migration pathways between UiO-66-NH_2 and Pd single atoms anchored g-C_3N_4 (48CN/Pd) using the *in situ* KPFM technique. As shown in Fig. 3d and g, the surface potential difference of the Si slice was −52.76 mV between dark and light conditions, which were applied as the background to avoid the influence of light. In Fig. 3e and h (line B), the surface potential of UiO-66-NH_2 decreased by −11.64 mV after light irradiation, revealing that photogenerated electrons accumulated on UiO-66-NH_2 under light irradiation. In addition, the surface potential of 48CN/Pd increased by 16.26 mV once light was turned on (line C, Fig. 3f and i), suggesting that the photogenerated electrons moved from 48CN/Pd to UiO-66-NH_2 under light conditions. Moreover, this technique has been applied in different systems such as TiO_2@UiO-66 composite[65] and UiO-66-NH_2@BiOI[66] for the investigation of the underlying photocatalytic mechanisms. Overall, KPFM is a well-developed technique that can be applied in the photocatalytic CO_2 reduction process for studying the electron-transfer pathways and product generation mechanisms.

5.3 Femtosecond transient absorption spectroscopy (fs-TA)

Femtosecond transient absorption spectroscopy (fs-TA), which is an advanced technique that combines time-resolved pump-probe technology with absorption spectroscopy, enables the detection of ultrafast interfacial charge-transfer signals at catalyst interfaces. The relaxation kinetics of photogenerated carriers from the ground state to the excited state can be simulated on femtosecond and picosecond time scales by analyzing the signals through fs-TA, which can provide direct evidence for the charge-transfer pathways during the photocatalytic process.[67] For instance, Cai *et al.*[68] confirmed the charge-transfer pathways in the $ZnIn_2S_4$/UiO-66-NH_2 nanocomposite through the fs-TA technique. In Fig. 4a and b, the negative peak at around 450–500 nm was related to the ground-

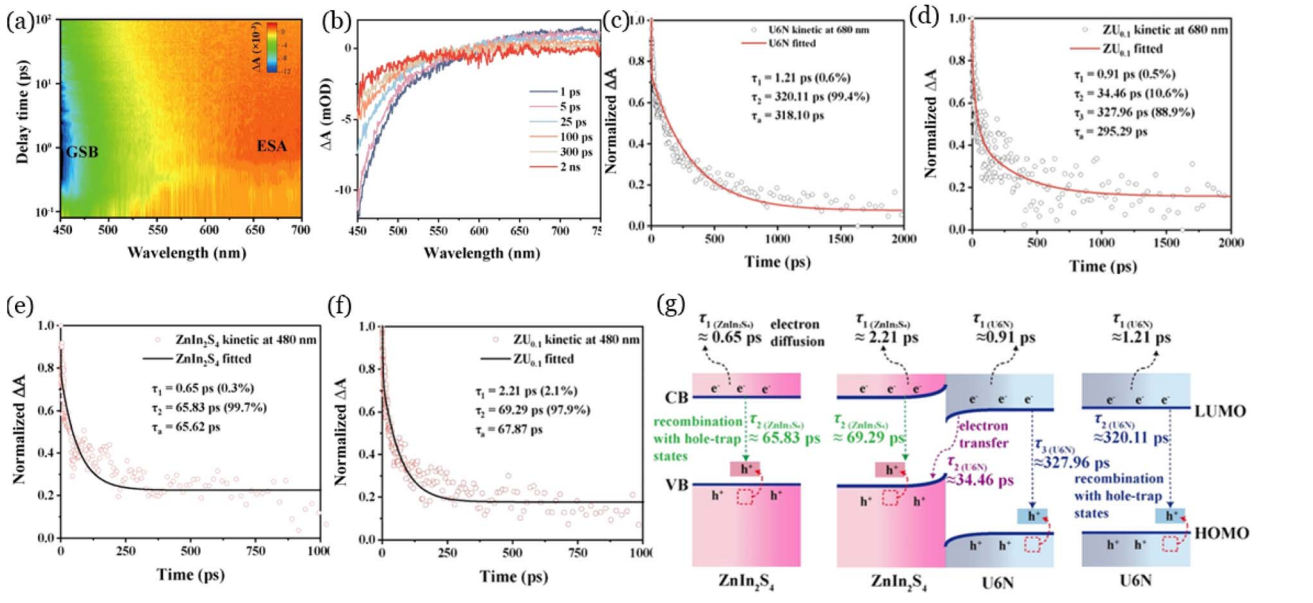

Fig. 4 Contour maps of fs-TA of $ZnIn_2S_4$/UiO-66-NH_2 ($ZU_{0.1}$) (a), representative spectra of $ZU_{0.1}$ at different delay time (b), excited-state absorption recovery kinetics of UiO-66-NH_2 (U6N) (c) and $ZU_{0.1}$ (d) probed at 680 nm, ground-state bleach recovery kinetics of $ZnIn_2S_4$ (e) and $ZU_{0.1}$ (f) probed at 480 nm, and schematic diagram of the charge transfer pathways (g), reproduced from ref. 68 with permission from Elsevier, copyright 2024.

state bleach (GSB) signal, and the positive peak at around 600–700 nm corresponded to the excited-state absorption (ESA) signal. In Fig. 4c, the two lifetimes from the fitted recovery kinetics results of UiO-66-NH_2 represent the electron diffusion in the crystal structure (τ_1), and the recombination of electrons and holes (τ_2), respectively. In Fig. 4d, the τ_1 (0.91 ns) and τ_3 (327.96 ns) of $ZnIn_2S_4$/UiO-66-NH_2 were close to the τ_1 (1.21 ns) and τ_2 (320.11 ns) of UiO-66-NH_2, suggesting that the composite nanomaterials presented electrons diffusion and recombination behaviors. The τ_2 (34.46 ns) of $ZnIn_2S_4$/UiO-66-NH_2 corresponded to the electron transfer on the surface of nanomaterials. Similarly, the τ_1 (0.65 ns) and τ_2 (65.83 ns) of $ZnIn_2S_4$ were close to the τ_1 (2.21 ns) and τ_2 (69.29 ns) of $ZnIn_2S_4$/UiO-66-NH_2 (Fig. 4e and f), indicating that only electron diffusion and recombination occurred in $ZnIn_2S_4$. Collectively, the results confirmed that the electrons moved from UiO-66-NH_2 to $ZnIn_2S_4$, as presented in Fig. 4g. Furthermore, fs-TA as a direct technique has been reported to be useful for investigating the underlying mechanisms in different systems, such as UiO-66-NH_2/$Cs_2AgBiBr_6$ for photocatalytic reduction of CO_2,[69] Au@UiO-66-NH_2/CdS for photocatalytic hydrogen evolution,[70] UiO-66-NH_2 for photocatalytic oxidation of nitric oxide.[71]

5.4 Electron paramagnetic resonance spectroscopy (EPR)

Electron paramagnetic resonance spectroscopy (EPR) is an indirect technique that can be used for assessing unpaired electrons. After the addition of spin-trapping agents to the system, the types and relative concentrations of generated paramagnetic species can be detected by EPR.[72] In general, 5,5-dimethyl-1-pyrroline *N*-oxide (DMPO) can be applied for the capture of $^{\bullet}OH$, $SO_4^{\bullet-}$, and $O_2^{\bullet-}$ radicals, and 2,2,6,6-tetramethylpiperidine (TEMP) can capture $^1O_2$.[73] This technique has been applied in the photocatalytic CO_2 reduction process for studying the charge-transfer pathways. Yuan *et al.*[74] observed that all the synthesized nanomaterials (UiO-66-NH_2, $Ce(HCOO)_3$, UiO-66-NH_2/$Ce(HCOO)_3$) were not able to produce $^{\bullet}OH$ radicals under dark conditions (Fig. 5a), while $^{\bullet}OH$ radicals were generated by UiO-66-NH_2 under light conditions (Fig. 5b). In Fig. 5c, the valence band position of $Ce(HCOO)_3$ was 1.89 V, which was more negative than $OH^-/^{\bullet}OH$ (2.4 V), suggesting that $Ce(HCOO)_3$ could not produce $^{\bullet}OH$. Because no $^{\bullet}OH$ radicals being detected in UiO-66-NH_2/$Ce(HCOO)_3$ under light conditions, all the holes from UiO-66-NH_2 were presumably transferred to $Ce(HCOO)_3$. Meanwhile, all the photogenerated electrons from $Ce(HCOO)_3$ moved to UiO-66-NH_2 for the efficient separation of photogenerated electron and hole pairs (Fig. 5d), achieving a high efficiency of photoreduction of CO_2. This technique has also been applied to various photocatalytic systems, such as g-C_3N_4/MoS_2,[76] NiO/BiOCl,[77] UiO-66-NH_2/g-C_3N_4,[78] for studying the mechanisms of photocatalytic CO_2 reduction.

5.5 Density functional theory (DFT) calculation

Density functional theory (DFT) is a computational method that can be used for the evaluation of electronic structures, work functions, band structures, adsorption sites and energy of semiconductors.[79] The electron-transfer pathways during the photocatalytic process can also be confirmed through DFT calculation of the work functions of photocatalysts. Zeng *et al.*[75] reported that the work functions (Φ) of UiO-66-NH_2 (001) and $Bi_7O_9I_3$ (110) were 5.27 V and 5.08 V, respectively (Fig. 5e and f). Leveraging the relationship between vacuum level (E_{vac}) and Fermi level (E_F) ($\Phi = E_{vac} - E_F$), the Fermi levels of two photocatalysts are presented in Fig. 5g. It is obvious that UiO-66-NH_2 exhibited a lower Fermi level compared to $Bi_7O_9I_3$, indicating that the photogenerated electrons from UiO-66-NH_2 moved to $Bi_7O_9I_3$ for the formation of S-scheme heterojunction (the mechanisms of S-scheme are discussed in the following

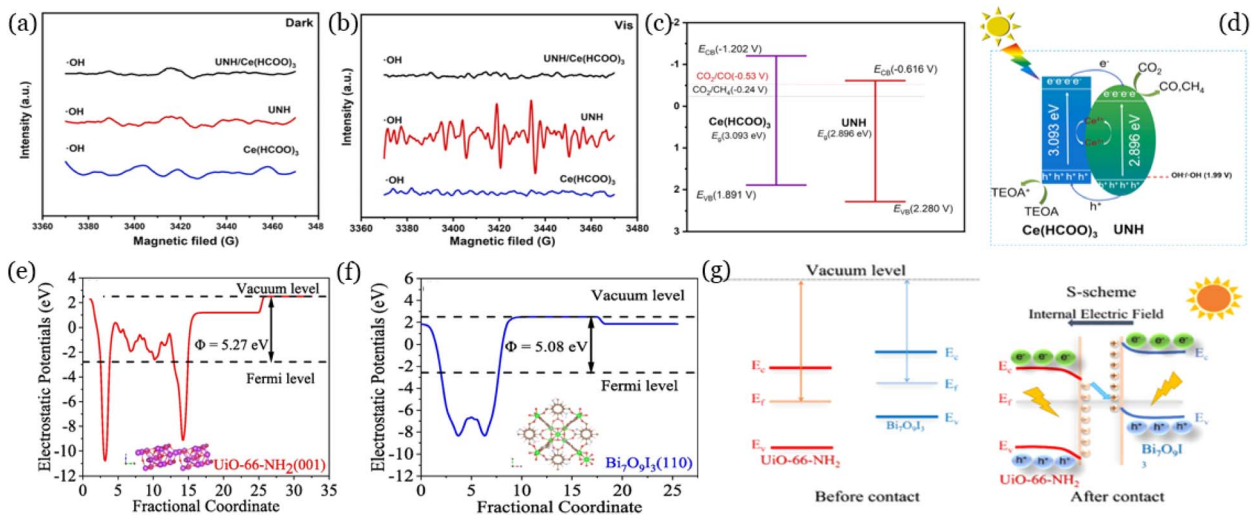

Fig. 5 EPR spectra for $^{\bullet}OH$ under dark condition as a control (a) and illumination (b) for UiO-66-NH_2 (UNH), $Ce(HCOO)_3$, and UNH/$Ce(HCOO)_3$, the band structure of UNH and $Ce(HCOO)_3$ (c), and schematic illustration of the photocatalytic reduction of CO_2 by UNH/$Ce(HCOO)_3$ composites (d), reproduced from ref. 74 with permission from Elsevier, copyright 2022. Work functions of UiO-66-NH_2 (001) (e) and $Bi_7O_9I_3$ (110) (f), schematic diagram of the S-scheme transfer pathway (g), reproduced from ref. 75 with permission from Elsevier, copyright 2023.

section). In summary, the calculation of work functions through DFT has been widely used for the identification of the charge-transfer pathways in different photocatalysts (*e.g.*, UiO-66-NH_2/SiC,[80] UiO-66-NH_2/CuZnS[81]) during the photocatalytic CO_2 reduction process.

6. Functional strategies for improving photocatalytic CO_2 reduction efficiency through UiO-66

As discussed earlier, several key parameters, including separation efficiency of photogenerated electron pairs, light absorption efficiency, CO_2 adsorption capacity, and electron transfer efficiency, can significantly affect the photocatalytic CO_2 reduction efficiency by UiO-66. Therefore, different efficiency enhancement strategies are critically discussed here, including surface functionalization, element doping, defect engineering, the addition of supporter, construction of heterojunctions, and dye sensitization.

6.1 Functionalization of organic linker

The organic linker of BDC can be easily functionalized by different functional groups (*e.g.*, NH_2, COOH) for the synthesis of functional UiO-66. In general, the modified UiO-66 confers high CO_2 adsorption capacity, excellent light harvesting efficiency, and outstanding separation efficiency for photogenerated electrons and holes. Aminated UiO-66 (UiO-66-NH_2) is the most reported and studied material, because it is well-acknowledged to have high stability and low energy band gap (around 2.8 eV),[82] which augments the photocatalytic efficiency under visible light. In addition, carboxylated UiO-66 (UiO-66-$(COOH)_2$) typically demonstrates high chemical stability (especially in acidic conditions) and excellent CO_2 adsorption capacity through the formation of hydrogen bonds between the materials and CO_2,[83] which is conducive to the photocatalytic CO_2 reduction process. Unfortunately, UiO-66-$(COOH)_2$ exhibits a wide band gap of around 3.6 eV, which means that it can only use ultraviolet light for photocatalysis.[84] Furthermore, it has also been reported that UiO-66-$(SH)_2$ exhibits excellent separation efficiency of photogenerated electrons and holes during photocatalysis.[85]

Although the functionalization of organic linkers can improve the properties of UiO-66, their performance is not satisfactory for photocatalytic CO_2 reduction. Therefore, the combination of different modifications for UiO-66, such as defect engineering of UiO-66-NH_2, and fabrication of UiO-66-NH_2-based heterojunction, are needed for efficient photoreduction of CO_2. Details are discussed in the following section.

6.2 Metallic element doping

Metallic element doping of UiO-66 is another efficient way to improve photocatalytic CO_2 reduction performance, by not only adjusting the energy band structure, but also increasing the separation efficiency of photogenerated electrons and holes by altering the electron-transfer pathway.[86] As illustrated in Fig. 6a, Zhu *et al.*[87] prepared Ni-doped UiO-66-NH_2 through a simple solvothermal process for efficient photocatalytic CO_2 reduction (CO yield of 3.7 μmol g^{-1} h^{-1}). They observed that Ni doping could change the energy band structure of UiO-66-NH_2 (Fig. 6b), mainly due to Ni^{2+} replacing Zr^{4+} in UiO-66-NH_2, leading to

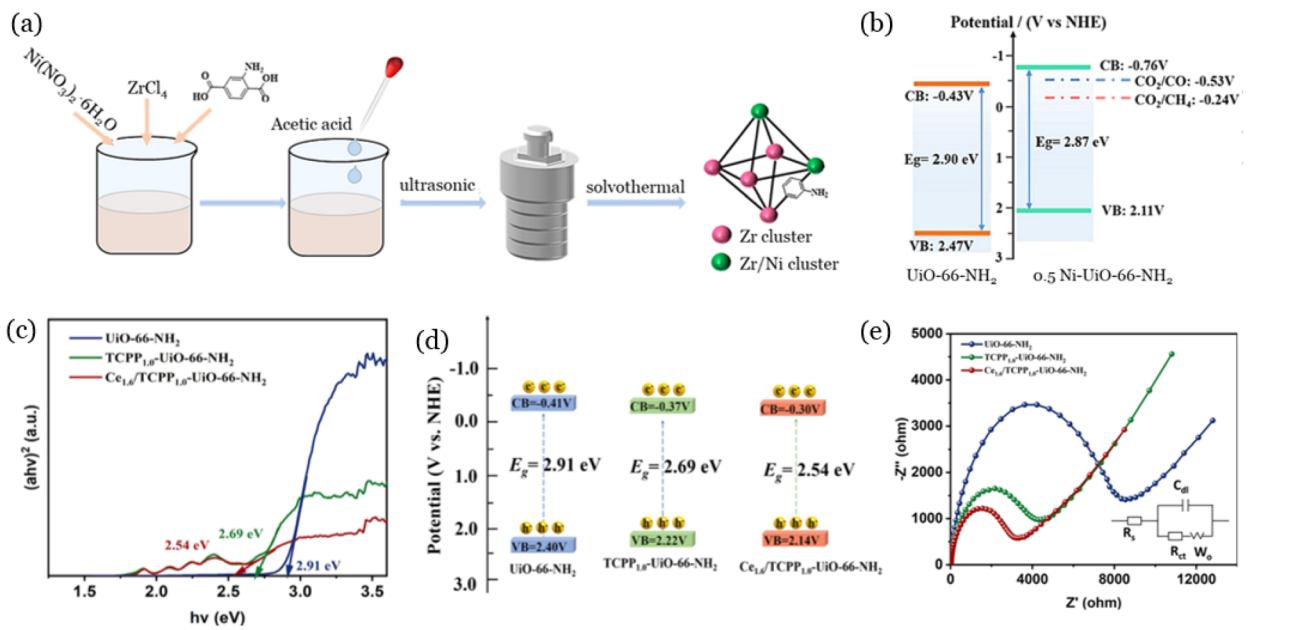

Fig. 6 Schematic illustration of the synthesis process of UiO-66-NH_2 (Zr/Ni) (a), energy band structures of UiO-66-NH_2 and 0.5 Ni-UiO-66-NH_2 (b), reproduced from ref. 87 with permission from Elsevier, copyright 2024. Tauc-plot (c), energy band structure (d), and electrochemical impedance spectroscopy (e) of UiO-66-NH2, TCPP1.0-UiO- 66-NH_2 and Ce1.6/TCPP1.0-UiO-66-NH_2, reproduced from ref. 88 with permission from Elsevier, copyright 2024.

changes in the electronic structure of the material. It was also confirmed that the separation efficiency of photogenerated electrons and holes by Ni-doped UiO-66-NH_2 increased due to the new metal-to-metal electron-transfer pathway. Similarly, Guo *et al.*[88] proved that Ce-doping in UiO-66-NH_2 could decrease the band gap of materials, resulting in excellent visible light absorption capacity (Fig. 6c and d). In Fig. 6e, the electrochemical impedance spectroscopy results confirmed that the Ce-doped UiO-66-NH_2 had the lowest resistance, indicating the highest separation efficiency of photogenerated electrons and holes among the prepared materials. In addition to single metallic element doping of UiO-66, multimetallic UiO-66 has also been reported recently. As an example, UiO-66 (Zr/Ce/Ti)-supported RuO_x nanoparticles have been applied for the photocatalytic CO_2 conversion in gas phase, exhibiting the highest activity compared with mono-(UiO-66 (Zr) or UiO-66 (Ce)) and bimetallic (UiO-66 (Zr/Ce) or UiO-66 (Zr/Ti))-based photocatalysts.[89]

Although different metallic elements such as Cu, Fe, and Co have been applied for the improvement of the properties of UiO-66 for photodegradation, the research on metallic element doping of UiO-66 for photocatalytic CO_2 reduction mainly focuses on Ni and Ce, which is mainly because the obtained materials demonstrate high CO_2 adsorption capacity and excellent separation efficiency of photogenerated carriers.

6.3 Defect engineering

Very recently, theoretical calculations proved that the presence of defects in UiO-66 could effectively improve the photocatalytic CO_2 reduction performance, mainly because the defects in UiO-66 could adjust the energy band structures and increase the separation efficiency of photogenerated carriers.[90] For instance, He *et al.*[91] prepared UiO-66 with missing linker defects by using acetic acid as the modulator. They observed that the defects in UiO-66 can reduce their band gap, increase the chemisorption capacity of CO_2, as well as improve the separation efficiency of photogenerated electrons and holes, which are beneficial for photocatalytic CO_2 reduction. In addition to the missing linker defects, missing linker clusters of UiO-66 are also effective for improving their performance. As shown in Fig. 7a, four types of UiO-66-NH_2 with different defects (missing linker defects and missing cluster defects) were synthesized for photocatalytic CO_2 reduction.[92] It was shown that the defects could adjust the energy band structures of UiO-66-NH_2 (Fig. 7b). Specifically, UiO-66-NH_2-LV demonstrated the most negative conduction band position compared with all the prepared nanomaterials, revealing the high efficacy for photoreduction of CO_2. DFT calculation and experimental results confirmed that ligand defects in UiO-66 could reduce the photocatalytic reaction energy barrier and increase visible light absorption, as well as serve as an active site to inhibit the recombination of photogenerated electrons and holes. Furthermore, oxygen vacancy, as a kind of defect in nanomaterials, has been demonstrated to improve the efficiency of photocatalysis. As discussed previously, the metallic element doping in UiO-66 could improve the efficiency of photocatalytic CO_2 reduction. Recent research further proved that the metallic element doping in UiO-66 could produce abundant oxygen vacancies. As an example, Xie *et al.*[94]

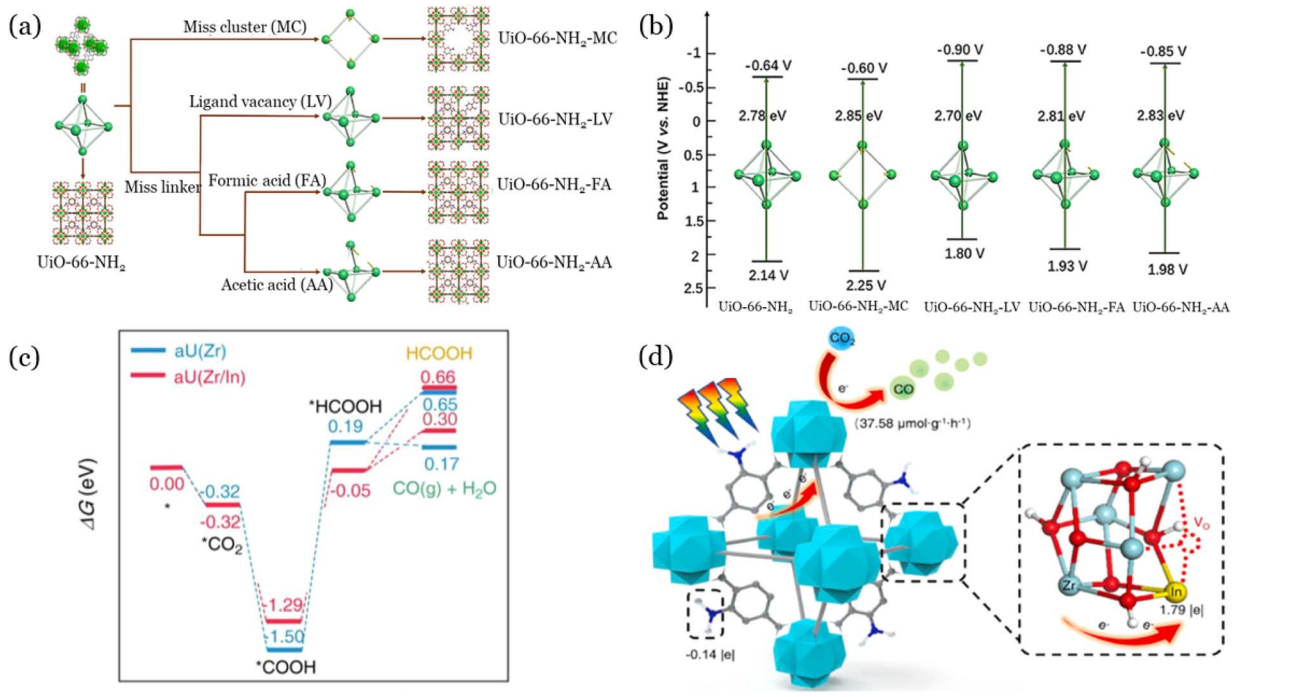

Fig. 7 Schematic illustration (a) and the band structure (b) of various defective structures of UiO-66-NH_2; reproduced from ref. 92 with permission from Elsevier, copyright 2022. Free energy of CO_2 reduction reaction pathways by aU(Zr) and aU(Zr/In) (c), proposed mechanism for photocatalytic CO_2 reduction by aU(Zr/In) (d); reproduced from ref. 93 with permission from Elsevier, copyright 2023.

observed that the Ce-doped UiO-66-NH_2 promoted the generation of oxygen vacancies on the surface of the nanomaterials, which could increase visible light absorption and accelerate separation of photogenerated electrons and holes, which in turn are conducive to the photoreduction of CO_2. In addition, Su *et al.*[93] also synthesized UiO-66 with plenty of oxygen vacancies through the indium (In) element doping process for CO_2 photoreduction under visible light. They proved that the In-doping could reduce the energy barrier of the intermediates during photocatalytic CO_2 reduction (Fig. 7c), and the oxygen vacancies could inhibit the recombination of photogenerated electron pairs. The synergistic effects of In-doping and oxygen vacancy resulted in excellent CO production efficiency during the photoreduction of CO_2 (Fig. 7d). Notably, Gibbs free energy (ΔG, Fig. 7c) was calculated using DFT to explore possible reaction pathways in the photocatalytic CO_2 reduction process, offering new insights into the underlying mechanisms. Beyond Gibbs free energy and work function (Section 5.5) calculations, DFT can be also applied to study various material properties, including the electronic and energy structures of photocatalysts, adsorption/desorption behavior, as well as reaction pathways with intermediates during photocatalytic CO_2 reduction.[79,95] For instance, Yang *et al.*[96] analyzed the electronic structure and Gibbs free energy of UiO-66/Co_9S_8 during photocatalytic CO_2 reduction, concluding that high-electron-density Co1 sites serve as the dominant active sites.

6.4 Addition of supporter

The agglomeration of UiO-66 is undesirable because it reduces the specific surface area and active sites of nanomaterials, resulting in relatively low efficiency for the photoreduction of CO_2. To address this, it has been confirmed that adding a supporter with a higher surface area can evenly distribute UIO-66 and prevent their agglomeration. Carbon nanotubes (CNTs) and graphene are the two most used supporters for photocatalytic CO_2 reduction mainly because of their large specific surface area, high porosity and excellent conductivity. As illustrated in Fig. 8a–c, the SEM results confirm that the UiO-66-NH_2 were uniformly deposited on the surface of CNTs, leading to more active sites being exposed for the adsorption of CO_2.[97] They also proved that CNTs in UiO-66-NH_2/CNTs increased electron mobility and suppressed the recombination of photogenerated electrons and holes, which were beneficial for the photoreduction of CO_2. As another example, Wang *et al.*[98] observed that graphene acted as a carrier that could effectively and evenly distribute UiO-66-NH_2 and Au particles (Fig. 8d and e), thereby enhancing the ability to adsorb CO_2. In addition, the graphene sheets could accept electrons to improve the separation efficiency of electron and hole pairs, and Au particles could also improve light absorption (through surface plasmon resonance), and inhibit the recombination of photogenerated electrons and holes by capturing the photoelectrons (Fig. 8f). These synergistic effects resulted in excellent CO_2 reduction efficiency and selectivity (80.9%) by Au/UiO-66-NH_2/graphene. Furthermore, Zhao *et al.*[99] reported that the covalent band between graphene oxide and UiO-66-NH_2 played a key role in efficient photoreduction of CO_2. The covalent band could not only quickly transfer the photoelectrons to graphene oxides, but also suppress the recombination of photogenerated electrons and holes by leveraging the electric field and potential difference. It should also be noted that CNTs and graphene oxides are expensive, which can increase the overall costs of the synthesized nanomaterials. Hence, some inexpensive supporters with

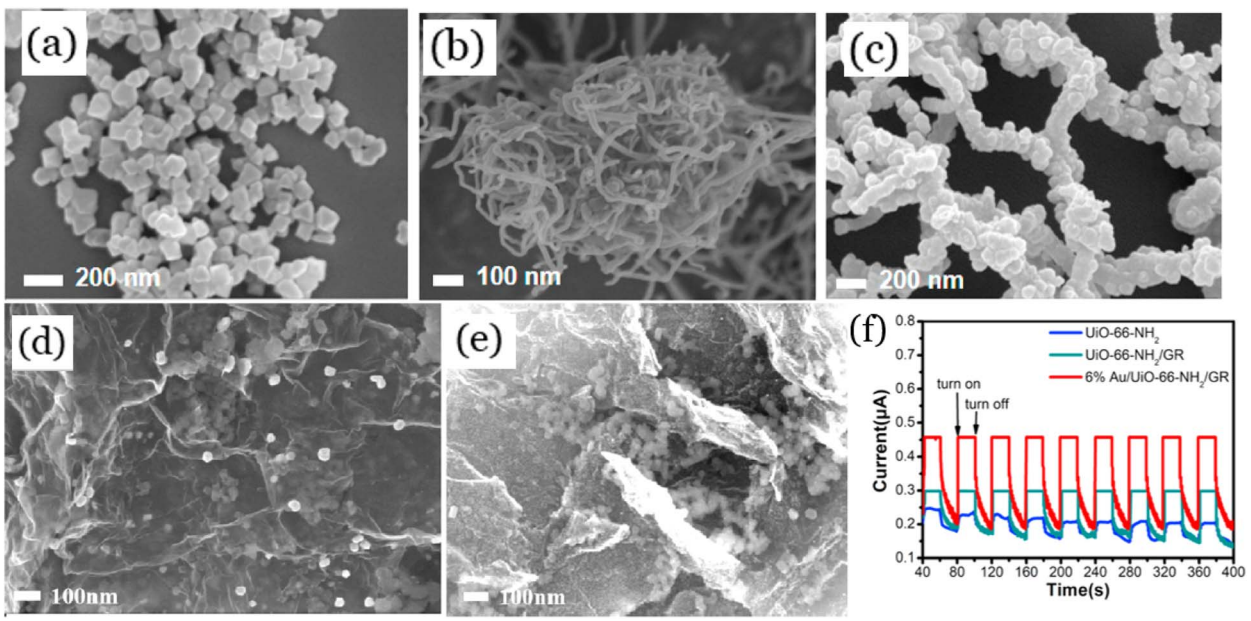

Fig. 8 SEM images of UIO-66-NH_2 (a), CNTs (b), and UIO-66-NH_2/CNTs (c), reproduced from ref. 97 with permission from Elsevier, copyright 2020. SEM images of UIO-66-NH_2/graphene (GR) (d) and Au/UIO-66-NH_2/GR (e), and photocurrent spectra of the prepared materials (f), reproduced from ref. 98 with permission from Elsevier, copyright 2021.

excellent properties are highly desired for the preparation of UIO-66-based catalysts for photocatalytic CO_2 reduction.

6.5 Construction of heterojunction

The fabrication of heterojunction between UiO-66 and another photocatalyst is promising for the efficient separation of photogenerated electron and hole pairs to further improve the efficiency of CO_2 photoreduction. In general, depending on the transfer pathways of electrons and involved mechanisms, the heterojunctions between two photocatalysts can be mainly classified into type I, type II, all-solid-state Z-scheme, direct Z-scheme, and S-scheme.[100] As illustrated in Fig. 9a, the electrons and holes are generated by two photocatalysts under light irradiation, and then the electrons and holes transfer from the photocatalyst with a high energy level to the photocatalyst with a low energy level. Meanwhile, the electrons and holes are accumulated on the conduction band and valence band of the semiconductor with low energy, respectively.[101] Firoozabadi *et al.*[102] observed that the type I heterojunction of TiO_2/UiO-66 could efficiently photocatalytically reduce CO_2 to give a high production rate of CH_4 (41.81 μmol g^{-1} h^{-1}) and CH_3OH (1.58 μmol g^{-1} h^{-1}). The strong bonding between TiO_2 and UiO-66 results in high CO_2 adsorption capacity and outstanding separation efficiency of electrons and holes, leading to an excellent CO_2 photoreduction efficiency. However, the type I heterojunction tends to encourage recombination of photogenerated electrons and holes on semiconductors with low positions of conduction band and valence band. To address this, the type II heterojunction has been shown to be more efficient for the separation of electrons and holes compared to the type I heterojunction.[103] In Fig. 9b, the electrons are transferred to the photocatalyst with a relatively low level of conduction band position, and the holes are moved to the photocatalyst with a low valence band position. Hence, the photoelectrons and holes are accumulated on two separate semiconductors, which effectively inhibits the recombination of electrons and holes.[104] For instance, Liu *et al.*[105] observed that the type II heterojunction of $HTiNbO_5$/UiO-66 composite demonstrated a higher CO production during photocatalytic CO_2 reduction of 9 and 11 times compared with UIO-66 and $HTiNbO_5$, respectively. They also proved that excellent CO_2 photoreduction efficiency was related to the improved light adsorption capacity and increased separation efficiency of photo-excited carriers. Hong *et al.*[106] also revealed that the large specific surface area and efficient separation efficiency of photogenerated electrons and holes in the UIO-66-NH_2/$CdIn_2S_4$ type II heterojunction resulted in high CO_2 photoreduction efficiency (CO = 11.2 μmol g^{-1} h^{-1}, CH_4 = 2.9 μmol g^{-1} h^{-1}). Furthermore, different type II heterojunctions, such as g-C_3N_4/UiO-66,[107] $Bi_4O_5Br_2$/UiO-66,[108] $Ce(HCOO)_3$/UiO-66-NH_2,[74] and MIL-101/UiO-66-NH_2,[109] have been reported to exhibit high efficiency for the photocatalytic reduction of CO_2, as summarized in Table 1.

Although type II heterojunctions can suppress the recombination of photogenerated electrons and holes, the holes and electrons are separately accumulated in the photocatalysts with a relatively lower conduction band and valence band position, respectively, which results in a low redox ability for photocatalysis. In contrast, Z-scheme heterojunctions can maintain high redox capacity. In all-solid-state Z-scheme heterojunctions (Fig. 9c), the photogenerated electrons from one semiconductor with a relatively lower conduction band position recombine with holes from another semiconductor with a relatively lower valence band position in the mediator. Hence, the photogenerated electrons and holes are accumulated on the conduction band and valence band, respectively, giving high redox abilities.[115] Noble metal nanoparticles (such as Pt, Ag, or

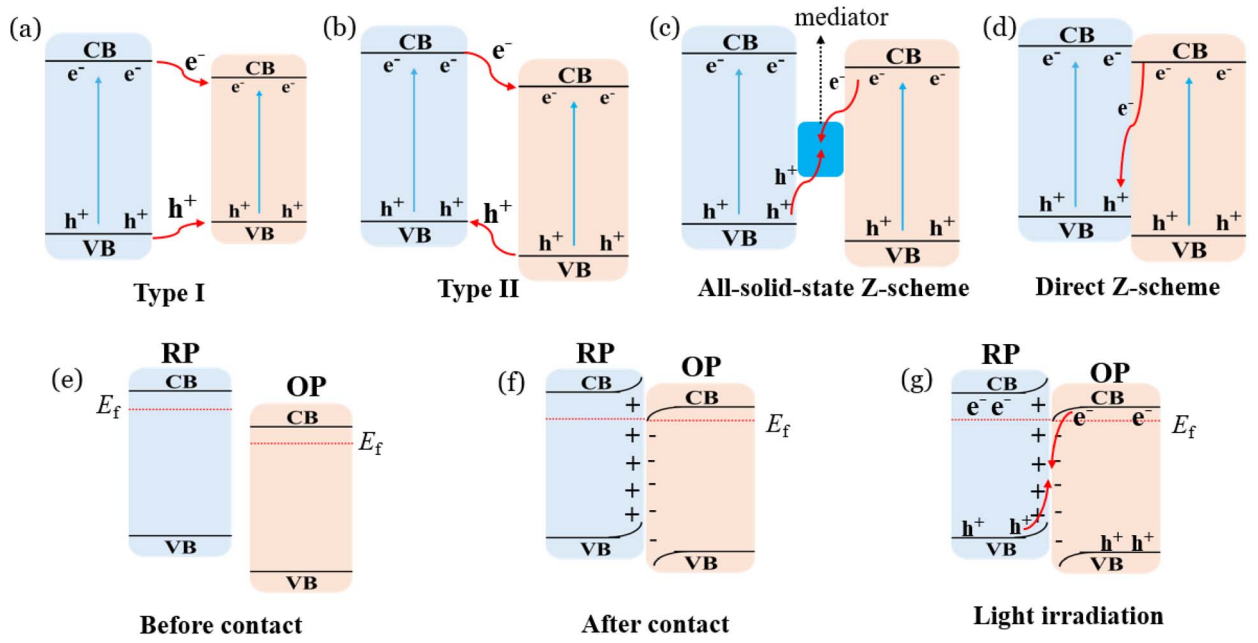

Fig. 9 Mechanisms of type I (a), type II (b), all-solid-state Z-scheme (c), direct Z-scheme (d), and S-scheme (e–g) heterojunctions.

Table 1 UiO-66 based heterojunctions for the photoreduction CO_2

Heterojunctions	Photocatalysts	Light source	Major products (μmol g^{-1} h^{-1})	Enhanced mechanisms	Ref.
Type II	g-C_3N_4/UiO-66	300 W Xe lamp (visible light intensity 660 mW cm^{-2})	CH_3OH = 54.7, C_2H_5OH = 38.1	Chemical bonds and close contact between two photocatalysts, concentrated photogenerated electrons	107
	$Bi_4O_5Br_2$/UiO-66	Xe lamp	CO = 8.35	Tight contact interface and electric field between two photocatalysts boosted separation efficiency of photogenerated electrons and holes	108
	$Ce(HCOO)_3$/UiO-66-NH_2	300 W Xe-lamp	CH_4 = 128.8	Expanded visible light absorption range, accelerated separation of photogenerated charges, multi-electron reduction reaction	74
	MIL-101/UiO-66-NH_2	300 W Xe-lamp	CO = 267.9, CH_4 = 18.3	Wide light absorption range, enhanced response to visible light, and increased reduction potential	109
Z-scheme	Cu_2O/Cu/UiO-66-NH_2	300 W Xe-lamp	CO = 4.54	Cu nanoparticles act as a mediator in the all-solid-state Z-scheme heterojunction, not only facilitating carrier transport, but also serving as an active site for CO_2 reduction	110
	CuO/Ag/UiO-66	300 W Xe-lamp	HCOOH = 61, CH_3OH = 5	Ag nanoparticles promote the separation of photogenerated electrons and holes, as well as exhibiting high capacity for adsorption of *H protons	111
	$Cs_2AgBiBr_6$/UiO-66	300 W Xe-lamp	CO = 15	Enhanced light-harvesting capacity and separation efficiency of photogenerated electrons, sufficient active sites	112
	MoS_2@UiO-66-NH_2	300 W Xe lamp (100 mW cm^{-2})	CH_4 = 27.1	Efficient charge transfer, large specific surface area	62
	Covalent organic frameworks-366 (Co)/UiO-66-NH_2	Simulated sunlight (light intensity 100 mW cm^{-2})	CO = 4000	Z-scheme heterojunction drives the charge transfer and enhances CO_2 photoreduction efficiency and selectivity	113
S-scheme	UiO-66-NH_2/CuZnS	300 W Xe-lamp	CO = 22.8	Abundant active sites, efficient separation of electrons and holes, outstanding photothermal effects	81
	Ce/Zr-UiO-66-NH_2/$CdIn_2S_4$	300 W Xe-lamp	CO = 6.01	Abundant oxygen vacancies, high electron transfer efficiency	114

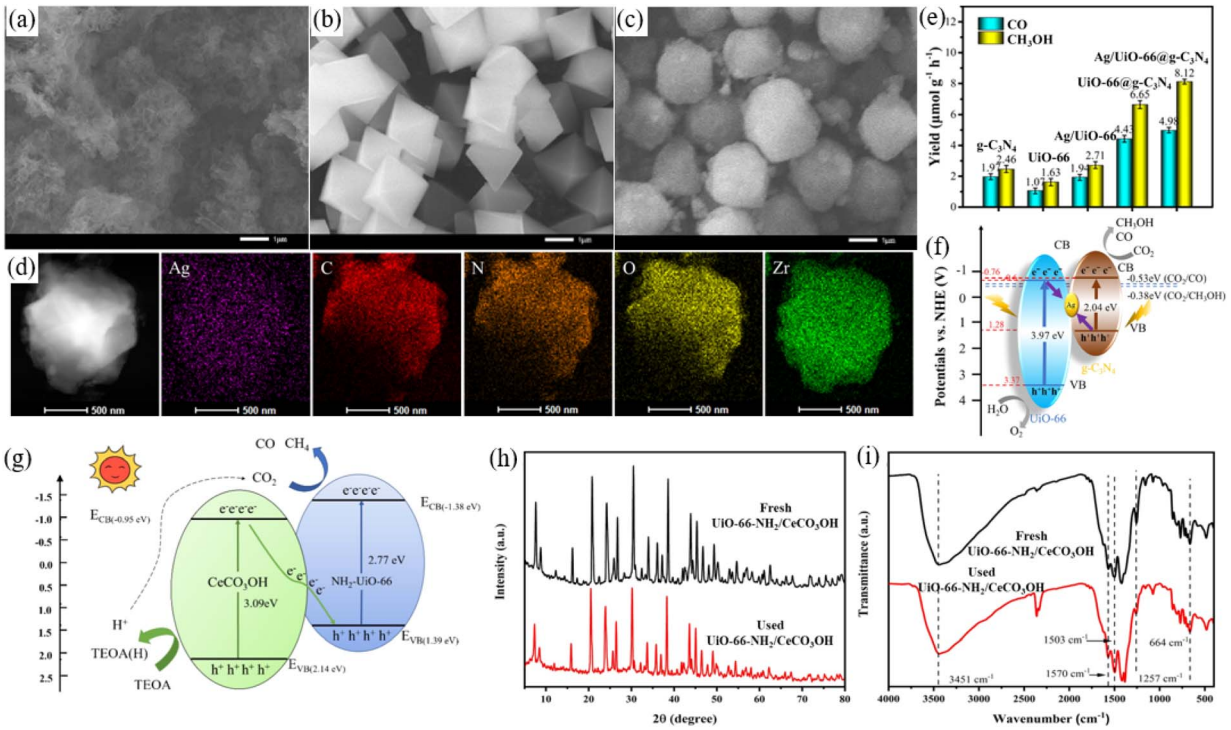

Fig. 10 SEM images of g-C_3N_4 (a), UIO-66 (b), and Ag/UiO-66@g-C_3N_4 (c), the mapping images (d) of Ag/UiO-66@g-C_3N_4, the activity of CO_2 photoreduction for photocatalysts (e), and charge transfer mechanism in Ag/UiO-66@g-C_3N_4 (f), reproduced from ref. 117 with permission from Elsevier, copyright 2023. Schematic diagram of the direct Z-scheme heterojunction of UIO-66-NH_2/$CeCO_3OH$ (g), the XRD patterns (h) and FTIR spectra (i) of fresh and used UiO-66-NH_2/$CeCO_3OH$, reproduced from ref. 118 with permission from Elsevier, copyright 2022.

Au) and carbon-based materials (such as carbon nanotubes and graphene) have been proven to serve as a mediator in the all-solid-state Z-scheme heterojunctions.[116] This type of heterojunction has been also applied in the UiO-66-based photocatalysts for photocatalytic reduction of CO_2. As illustrated in Fig. 10a–d, the SEM and mapping results confirmed that Ag/UiO-66@g-C_3N_4 nanocomposites were successfully synthesized. The Ag/UiO-66@g-C_3N_4 demonstrated the highest CO and CH_3OH production yield among all the prepared nanocomposites (Fig. 10e), which were mainly due to the Ag nanoparticles as the mediator could promote the separation of electrons and holes, as well as maintain the high redox potential for the photocatalytic reduction of CO_2 (Fig. 10f).[117] In addition, the Z-scheme heterojunctions of Cu_2O/Cu/UiO-66-NH_2 (ref. 110) and CuO/Ag/UiO-66 (ref. 111) have been also demonstrated to be efficient for the photoreduction of CO_2. Furthermore, the electrons from one photocatalyst can directly recombine with the holes from another photocatalyst (without a mediator) for the formation of direct Z-scheme heterojunctions (Fig. 9d), which can also retain their high redox potential.[119] As illustrated in Fig. 10g, the photogenerated electrons from $CeCO_3OH$ are recombined with holes from UiO-66-NH_2 to promote the separation of carriers and retain their high redox potential in the direct Z-scheme heterojunction.[118] The XRD patterns (Fig. 10h) and FTIR spectra (Fig. 10i) of fresh and used Z-scheme heterojunction of UiO-66-NH_2/$CeCO_3OH$ confirmed that it had high stability for the photocatalytic reduction of CO_2. Additionally, the direct Z-scheme heterojunctions, such as $Cs_2AgBiBr_6$/UiO-66,[112] and MoS_2@-UiO-66-NH_2,[62] have been reported to confer an improved efficiency of CO_2 photoreduction.

Furthermore, a relatively novel concept of S-scheme (step-scheme) heterojunction was introduced to clearly explain the involved mechanisms in 2019.[120] As illustrated in Fig. 9e–g, the S-scheme heterojunction normally contains an oxidation photocatalyst (OP) with a lower Fermi level and a reduction photocatalyst (RP) with a higher Femi level. When two photocatalysts come into contact under dark conditions, the electrons in RP spontaneously move to the surface of OP due to the difference in Fermi levels. When the Fermi levels between RP and OP reach equilibrium, the positively charged RP and negatively charged OP result in the formation of an internal electric field, which can lead to further downward band bending of OP and upward band bending of RP.[121] Under light irradiation, the RP and OP are excited for the generation of electrons and holes. Subsequently, the photogenerated electrons from OP recombine with holes from RP due to the internal electric field and energy band bending, and the photoelectrons from RP and holes from OP remained. Therefore, the S-scheme heterojunctions exhibit efficient separation efficiency of photogenerated electrons and holes, and excellent redox ability, during the photocatalytic process.[122] Xiao *et al.*[80] observed that the S-scheme heterojunction of UiO-66-NH_2/SiC demonstrated a high photocatalytic CO production of 7.3 μmol g^{-1} h^{-1}, which was 5 times that of pristine UiO-66-NH_2. This was mainly due to the larger specific surface area of the composite increasing the

Table 2 Functional strategies for improving the photocatalytic CO_2 reduction efficiency of UiO-66

Photocatalysts	Strategies	Light source	Major products (μmol g^{-1} h^{-1})	Enhanced mechanisms	Ref.
Ce-doped UiO-66-NH_2	Metallic element doping	Simulated sunlight (light intensity 90 mW cm^{-2})	CO = 30.4	Expanded micro- and mesoporous volumes, increased CO_2 adsorption capacity and light absorption, improved photogenerated carrier separation efficiency	128
UiO-66-NH_2/TiO_2/Au	Heterojunction	Solar lamp (300–800 nm, UV = 46 W m^{-2}, visible = 4271 W m^{-2})	CH_4 = 27.2	Abundant CO_2 adsorption sites, high visible light absorption capacity, large interface contact area	129
N-doped $HTiNbO_5$/UiO-66-NH_2	Heterojunction	Simulate solar (light intensity 500 mW cm^{-2})	CH_4 = 2.1, CO = 0.6	N sites lower the overall activation energy barrier and improve the separation and transfer of the photoinduced charge carriers	130
Cu single atom@ polymeric carbon nitride UiO-66-NH_2	Heterojunction, single-atom	300 W Xe-lamp (visible light)	CH_3OH = 4150	The formation of type-II heterojunction results in better charge separation, and Cu single atoms improve the catalytic performance	131
UiO-66-NH_2/$ZnIn_2S_4$	Heterojunction	300 W Xe-lamp (light intensity 200 mW cm^{-2})	CO = 57	Excellent CO_2 adsorption capacity, efficient charge transfer pathways, and tight interfacial contacts	132
Ni porphyrin-sensitized P25/UiO-66	Heterojunction	Simulate sunlight (light intensity 150 mW cm^{-2})	CO = 14.6	Improved electron–hole separation efficiency, and high visible light absorption capacity	133
UiO-66-NH_2/Au/In_2O_3	Heterojunction	300 W Xe-lamp	CO = 8.56	Widened light absorption, improved carrier separation and CO_2 adsorption capacity	134
UiO-66-MIL-125 (Ti)	Heterojunction	300 W Xe-lamp (light intensity 1472 mW cm^{-2})	CO = 56.4	The formation of type-II heterojunction results in better charge separation, exposed facet improves the adsorption and activation of CO_2	135
CdS@UiO-66-NH_2	Heterojunction	LED lamp	CO = 280.5	Enhanced separation and migration of photo-generated charge carriers, improved visible light absorption ability, large specific surface area, and abundant active sites	136
3D-graphene-UiO-66-NH_2	Addition of supporter	500 W Xe-lamp (λ > 400 nm)	HCOOH = 42.1 μmol	Enhanced CO_2 absorption and inhibited photogenerated charge recombination	137

adsorption capacity of CO_2, and the S-scheme heterojunction promoting the separation of photogenerated electrons and holes. In addition, different UiO-66-based S-scheme heterojunctions, such as UiO-66-NH_2/CuZnS[81] and Ce/Zr-UiO-66-NH_2/$CdIn_2S_4$,[114] have been also synthesized for the efficient photoreduction of CO_2, with the details summarized in Table 1.

6.6 Combination with single atom catalyst

In 2011, single isolated metal atoms stabilized on appropriate support were first reported by Qiao *et al.*[123] Subsequently, single-atom catalysts have received considerable attention in the catalytic research field due to their inherently beneficial properties such as excellent catalytic efficiency and selectivity, and maximum atom-utilization efficiency.[124] UiO-66, with a large specific surface area, has been considered an excellent support for the single atoms. Wang *et al.*[125] observed that Cu single atoms/UiO-66-NH_2 exhibited high methanol (5.3 μmol g^{-1} h^{-1}) and ethanol (4.2 μmol g^{-1} h^{-1}) production rates during CO_2 photoreduction under visible light irradiation. The results confirmed that the Cu single atoms enriched electrons and promoted a multi-electronic process, which facilitated the formation of CHO* and CO* intermediates, resulting in high selectivities of methanol and ethanol. Chu *et al.*[126] also reported that Zn single atoms/UiO-66-NH_2 displayed a high CO_2 reduction efficiency, which was mainly due to the formation of an electric field between Zn single atoms and UiO-66-NH_2, resulting in a high separation efficiency of photogenerated electrons and holes. In addition, single atoms can be attached to the surface of UiO-66 through the chelating agent. As an example, Co single atoms grafted UiO-66-NH_2 were synthesized by using ethylenediaminetetraacetic acid (EDTA) as binding sites through a one-pot synthesis process.[127] The high CO production of 776 μmol g^{-1} h^{-1} during CO_2 photoreduction was related to EDTA acting as an electron donor to provide extra electrons for the photoreduction of CO_2, as well as preventing the agglomeration of Co single atoms on the surface of UiO-66-NH_2. Hence, the combination of a single atom and UiO-66 can be an excellent method for improving CO_2 photoreduction efficiency.

Moreover, functional strategies to modify UiO-66 to improve photocatalytic CO_2 reduction efficiency are summarized Table 2. These advancements offer valuable insights for further augmenting UiO-66's potential for this purpose. Despite significant progress, product selectivity remains a key challenge requiring more in-depth investigation. Ali *et al.*[138] reported that product selectivity during photocatalytic CO_2 reduction is influenced by both thermodynamic and dynamic factors. Thermodynamic factors relate to photo energy and the CB and VB positions of the photocatalysts (Fig. 2a), while dynamic factors include light intensity, availability of photogenerated electrons and holes, active sites, adsorption and stabilization of reactants and intermediates, and CB and VB positions. In general, active sites with the appropriate photogenerated electron–hole density and adsorption/stabilization properties play a crucial role in determining can product selectivity.[139] In addition, Liao *et al.*[140] demonstrated that crystal plane designation, metal ion doping, surface plasmon resonance, and defect engineering can promote the generation of C_{2+} products by reducing reaction barriers, providing more active sites and photogenerated carriers. Overall, photocatalytic CO_2 reduction by UiO-66 to produce desired products is still in the early stages, and further innovations are needed to drive breakthroughs in this field.

7. Conclusions and perspectives

The photocatalytic CO_2 reduction into fuels has been recognized as a very promising technique to alleviate environmental problems (*i.e.*, reducing greenhouse gas emissions) and address the transition from fossil fuels (*i.e.*, carbon utilization). In this regard, UiO-66 as an outstanding MOF nanomaterial has been considered an excellent candidate for the photoreduction of CO_2, due to its high stability, large specific surface area, tunable pore size, and excellent CO_2 adsorption capacity. Therefore, the present review focuses on the state-of-the-art on photocatalytic CO_2 reduction by UiO-66. Firstly, the fundamentals and existing challenges of photocatalytic CO_2 reduction are summarized and critically reviewed, and then the history, advances, synthesis routines, challenges of UiO-66 are described. Subsequently, the charge-transfer pathway, which is one of the most important parameters that can significantly affects the photocatalytic performance, is elucidated, along with the techniques for characterization. Following that, different strategies for enhancing the photocatalytic CO_2 reduction efficiency by UiO-66 are overviewed, including functionalization of the organic linker, metallic element doping, defect engineering, addition of supporter, construction of heterojunction, and combination with a single-atom catalyst. Finally, the challenges and perspectives regarding photocatalytic CO_2 reduction are presented as follows.

(1) Most of the UiO-66 are synthesized through a conventional solvothermal process, which is not an economical and environmentally friendly method, because the reaction process requires high temperature and pressure, and relatively high-toxicity DMF is also needed. Recently, several alternative methods, such as mechanochemical synthesis,[141] microwave-assisted synthesis,[54] and electrochemical process,[55] have been developed for the preparation of UiO-66. These approaches show significant potential for the commercial production of UiO-66, though only a limited number of studies have explored these methods in detail. More facile, efficient, and sustainable methods are highly desired for the synthesis of UiO-66 in the future. Moreover, the parameters for evaluating a synthesis method, such as energy consumption and potential toxicity, should be thoroughly examined before commercialization. Additionally, a life cycle assessment (LCA) should be conducted to comprehensively evaluate the environmental impact.

(2) Although UiO-66 is among the most stable MOFs, its long-term stability remains largely unverified, particularly under harsh and real-world (non-ideal) conditions. Studies have shown that UiO-66 can degrade (*e.g.*, reduced crystallinity, porosity loss, partial dissolution, and loss of linker) under highly alkaline environments or in solutions containing coordinating ions (*e.g.*, bicarbonate, phosphate, and conjugate acids) due to the substitutional displacement of linker termini

from Zr-nodes.[26] To enhance its chemical stability, several strategies have been proven, including coating UiO-66-NH_2 with two-dimensional covalent organic frameworks,[142] synthesizing black phosphorus/UiO-66 composites,[143] and developing Mo_2C/UiO-66 composites.[144] However, further research is needed to assess UiO-66's performance under more realistic conditions, such as extreme pH levels and elevated temperatures, to fully evaluate its potential as practical photocatalysts. In addition, it has been proven that the metallic element doping and defect engineering of UiO-66 could significantly improve photocatalytic CO_2 reduction performance. On the other hand, such modifications also partially changed the original structures of UiO-66, which may compromise the stability of modified UiO-66 relative to pristine UiO-66. The present modifications for UiO-66 mainly focus on performance parameters (*e.g.*, specific surface area, photoreduction CO_2 efficiency, adsorption capacity), whereas the stability of modified UiO-66 receives limited attention. The stability of UiO-66 is an important property for commercial utilization and thus should be given more attention in future studies.

(3) Pristine UiO-66 can only absorb UV light due to the wide band gap, while modified UiO-66 can efficiently absorb visible light. For photocatalytic CO_2 reduction by UiO-66, most of the research studies were carried out under visible light with a relatively high light intensity (typically Xe lamp as light source, with a cut-off of 420 nm). The mechanisms of CO_2 photoreduction by UiO-66 may be different between visible light and sunlight. To utilize sunlight, the effects of the low light intensity and wavelength range need to be studied. In other words, more studies need to be dedicated to investigating CO_2 photoreduction by UiO-66 under solar light or simulated sunlight.

(4) Different modifications to UiO-66 have been made to improve photocatalytic CO_2 reduction efficiency. Although these methods could significantly enhance performance, the underlying mechanisms remains incompletely understood. It has been reported that modifications could positively change the properties of UiO-66, including separation efficiency of photogenerated electrons and holes, CO_2 adsorption capacity, availability of active sites, and light absorption capacity. However, which parameters are most critical and the interplay between these parameters have not been determined clearly. This is mainly because most of the modifications cannot precisely control any one property of UiO-66, so the resulting effects of many properties are convoluted. To address this, machine learning can play a useful role to evaluate the relative influences and guide modifications.

(5) While remarkable progress has been achieved for photocatalytic CO_2 reduction, more comprehensive understanding of the underlying mechanisms can further augment efficiency. Most characterization techniques (in Section 5) only study photocatalytic mechanisms indirectly, but *operando* characterizations would be much more valuable. At present, *operando* characterizations for photocatalytic CO_2 reduction are difficult due to the complexity of the reaction systems, relatively fast reaction and low concentration of products, as well as expensive instruments. For instance, *in situ* XPS can only be applied at relatively low pressure (<0.5 mbar). Hence, more efforts should be devoted to developing suitable *operando* characterization techniques. In addition, DFT calculation is also an important tool for unveiling photocatalytic CO_2 reduction mechanisms. The combination of DFT calculation and experimental results is beneficial for shedding light on the structure–property relationship of UiO-66 during photocatalytic CO_2 reduction.

(6) During the photocatalytic process, photogenerated electrons and holes are generated on the surface of the photocatalyst, and the side reaction of hole-based oxidation also occurs. At present, a scavenger (*e.g.*, triethanolamine, methanol, and ascorbic acid) is normally used for rapid consumption of the generated holes, which is not a sustainable and environmentally friendly method. In addition, the chemical stability of UiO-66 in the presence of scavengers remains a challenge. While reuse experiments and various characterizations have been conducted to assess the stability of used photocatalysts, these studies only ascertain short-term stability. Hence, further research is needed to evaluate the long-term chemical stability of UiO-66 for photocatalytic CO_2 reduction. As an alternative, the combination of CO_2 photoreduction and organic pollutants oxidation can be an excellent way to achieve a double-win photocatalytic process. Additionally, a hydrogen evolution reaction may also occur since plenty of water is involved in the main process in the solid–liquid mode, hence, the solid–gas mode (CO_2-saturated water vapor is typically fed directly or a minimal amount of water is added into the reactor) for CO_2 photoreduction is promising for future study. Furthermore, the main products of photocatalytic CO_2 reduction are C_1 compounds (*e.g.*, CO, CH_4), which are less valuable than C_{2+} products (*e.g.*, C_2H_5OH, C_2H_4). Therefore, means for directed production of desired products would be advantageous but remain challenging. Recently, it has been reported that the introduction of electric field or heating during CO_2 photoreduction can promote the generation of C_{2+} products, which warrants further study.

(7) Hitherto, most of the research on this topic has been carried out on the lab-scale and under ideal conditions, even though the performances of UiO-66 are expected to be quite different in real conditions. In addition, the efficiency of light harvesting is still low, which also inhibits performance. The yield of the products for CO_2 photoreduction is on the order of $\mu mol\ g^{-1}\ h^{-1}$, which is too low for practical application. While the reactor design is also crucial for optimal photocatalytic CO_2 reduction, only limited research focuses on the study of reactors. For instance, it has been reported that the two-chamber reactor gives higher CO_2 photoreduction efficiency compared to the traditional reactor. More research should be devoted to the design and scale-up of photocatalytic reactors.

Significant progress has been achieved in photocatalytic CO_2 reduction in recent years; however, much remains to be done before realizing its potential in practical applications. Despite the challenges, there is strong confidence that the ultimate goal of achieving a sustainable photoreduction process will be accomplished in the near future.

Data availability

No primary research results and no new data were generated as part of this review.

Author contributions

Yongtao Xue: investigation, methodology, visualization, writing – original draft. Jia Wei Chew: project administration, funding acquisition, writing – review & editing.

Conflicts of interest

There are no conflicts to declare.

Acknowledgements

This work was supported by Chalmers Gender Initiative for Excellence (Genie).

References

1 W. Wang, L. Wang, W. Su and Y. Xing, *J. CO_2 Util.*, 2022, **61**, 102056.
2 L. Tan, Y. Li, Q. Lv, Y. Gan, Y. Fang, Y. Tang, L. Wu and Y. Fang, *Catal. Today*, 2023, **410**, 282–288.
3 Z. Fang, Y. Hu, B. Yao, Z. Ye and X. Peng, *J. Mater. Chem. A*, 2024, **12**, 6112–6122.
4 H.-N. Wang, Y.-H. Zou, H.-X. Sun, Y. Chen, S.-L. Li and Y.-Q. Lan, *Coord. Chem. Rev.*, 2021, **438**, 213906.
5 J. L. Holechek, H. M. E. Geli, M. N. Sawalhah and R. Valdez, *Sustainability*, 2022, **14**(8), 4792.
6 W. Lai, Y. Qiao, Y. Wang and H. Huang, *Adv. Mater.*, 2023, **35**, 2306288.
7 S. Fang, M. Rahaman, J. Bharti, E. Reisner, M. Robert, G. A. Ozin and Y. H. Hu, *Nat. Rev. Methods Primers*, 2023, **3**, 61.
8 S. Kaur, M. Kumar, D. Gupta, P. P. Mohanty, T. Das, S. Chakraborty, R. Ahuja and T. C. Nagaiah, *Nano Energy*, 2023, **109**, 108242.
9 W. Wang, C. Zeng and N. Tsubaki, *Green Carbon*, 2023, **1**, 133–145.
10 P. Tyagi, D. Singh, N. Malik, S. Kumar and R. Singh Malik, *Mater. Today*, 2023, **65**, 133–165.
11 R. Gupta, A. Mishra, Y. Thirupathaiah and A. K. Chandel, *Biomass Convers. Biorefin.*, 2024, **14**, 3007–3030.
12 T. Qu, S. Wei, Z. Xiong, J. Zhang and Y. Zhao, *Fuel Process. Technol.*, 2023, **251**, 107933.
13 F. Zhou, Y. Zhang, J. Wu, W. Yang, X. Fang, T. Jia, Y. Ling, P. He, Q. Liu and J. Lin, *Appl. Catal., B*, 2024, **341**, 123347.
14 C.-H. Chiang, C.-C. Lin, Y.-C. Lin, C.-Y. Huang, C.-H. Lin, Y.-J. Chen, T.-R. Ko, H.-L. Wu, W.-Y. Tzeng, S.-Z. Ho, Y.-C. Chen, C.-H. Ho, C.-J. Yang, Z.-W. Cyue, C.-L. Dong, C.-W. Luo, C.-C. Chen and C.-W. Chen, *J. Am. Chem. Soc.*, 2024, **146**, 23278–23288.
15 S. Bai, W. Jing, G. He, C. Liao, F. Wang, Y. Liu and L. Guo, *ACS Nano*, 2023, **17**, 10976–10986.
16 X. Zhang, K. Matras-Postolek, P. Yang and S. P. Jiang, *Carbon*, 2023, **214**, 118337.
17 Y.-L. Dong, Y. Jiang, S. Ni, G.-W. Guan, S.-T. Zheng, Q. Guan, L.-M. Pei and Q.-Y. Yang, *Small*, 2024, **20**, 2308005.
18 Y.-L. Dong, H.-R. Liu, S.-M. Wang, G.-W. Guan and Q.-Y. Yang, *ACS Catal.*, 2023, **13**, 2547–2554.
19 W. Song, G. Qi and B. Liu, *J. Mater. Chem. A*, 2023, **11**, 12482–12498.
20 Z. Shang, X. Feng, G. Chen, R. Qin and Y. Han, *Small*, 2023, **19**, 2304975.
21 J. Liu, W. Qin, Y. Wang, Q. Xu, Y. Xie, Y. Chen, Y. Dai and W. Zhang, *Sep. Purif. Technol.*, 2024, **344**, 127289.
22 L. Zheng, H. Yang, M. Zhang, Z. Guan, Q. Li and J. Yang, *Chem.–Eur. J.*, 2024, **30**, e202402031.
23 S.-Q. Wang, X. Wang, X.-M. Cheng, J. Ma and W.-Y. Sun, *J. Mater. Chem. A*, 2022, **10**, 16396–16402.
24 Z. Fang, X. Yue and Q. Xiang, *Small*, 2024, **20**, 2401914.
25 H. Liu, M. Cheng, Y. Liu, G. Zhang, L. Li, L. Du, B. Li, S. Xiao, G. Wang and X. Yang, *Coord. Chem. Rev.*, 2022, **458**, 214428.
26 S. Daliran, A. R. Oveisi, C.-W. Kung, U. Sen, A. Dhakshinamoorthy, C.-H. Chuang, M. Khajeh, M. Erkartal and J. T. Hupp, *Chem. Soc. Rev.*, 2024, **53**, 6244–6294.
27 A. Dhakshinamoorthy, A. Santiago-Portillo, A. M. Asiri and H. Garcia, *ChemCatChem*, 2019, **11**, 899–923.
28 K. Guo, I. Hussain, G. Jie, Y. Fu, F. Zhang and W. Zhu, *J. Environ. Sci.*, 2023, **125**, 290–308.
29 T. Inoue, A. Fujishima, S. Konishi and K. Honda, *Nature*, 1979, **277**, 637–638.
30 K. Yang, Z. Yang, C. Zhang, Y. Gu, J. Wei, Z. Li, C. Ma, X. Yang, K. Song, Y. Li, Q. Fang and J. Zhou, *Chem. Eng. J.*, 2021, **418**, 129344.
31 J. Fu, K. Jiang, X. Qiu, J. Yu and M. Liu, *Mater. Today*, 2020, **32**, 222–243.
32 M. Wang, D. Chen, N. Li, Q. Xu, H. Li, J. He and J. Lu, *Adv. Mater.*, 2022, **34**, 2202960.
33 Q. Heng, B. Wang, X. Fan, W. Chen, X. Li, L. Mao and W. Shangguan, *J. Alloys Compd.*, 2022, **920**, 165945.
34 E. M. Cedeño Morales, B. I. Kharisov and M. A. Méndez-Rojas, *Mater. Today: Proc.*, 2021, **46**, 2982–2997.
35 H. Yang, *Mater. Res. Bull.*, 2021, **142**, 111406.
36 J. Song, Y. Lu, Y. Lin, Q. Liu, X. Wang and W. Su, *Appl. Catal., B*, 2021, **292**, 120185.
37 M. Yang, P. Wang, Y. Li, S. Tang, X. Lin, H. Zhang, Z. Zhu and F. Chen, *Appl. Catal., B*, 2022, **306**, 121065.
38 B. Khan, F. Raziq, M. Bilal Faheem, M. Umar Farooq, S. Hussain, F. Ali, A. Ullah, A. Mavlonov, Y. Zhao, Z. Liu, H. Tian, H. Shen, X. Zu, S. Li, H. Xiao, X. Xiang and L. Qiao, *J. Hazard. Mater.*, 2020, **381**, 120972.
39 X. Li, Y. Bai, X. Shi, J. Huang, K. Zhang, R. Wang and L. Ye, *Appl. Surf. Sci.*, 2021, **546**, 149111.
40 L. Liu, S. Wang, H. Huang, Y. Zhang and T. Ma, *Nano Energy*, 2020, **75**, 104959.
41 G. Li, Y. Sun, Q. Zhang, Z. Gao, W. Sun and X. Zhou, *Chem. Eng. J.*, 2021, **410**, 128397.

42 N. A. Ramsahye, J. Gao, H. Jobic, P. L. Llewellyn, Q. Yang, A. D. Wiersum, M. M. Koza, V. Guillerm, C. Serre, C. L. Zhong and G. Maurin, *J. Phys. Chem. C*, 2014, **118**, 27470–27482.
43 O. A. Koriem, M. S. Showman, A. H. El-Shazly and M. Elkady, *Cellulose*, 2024, **31**, 2309–2325.
44 M. Chen, J. Zeng, Z. Wu, R. Zhang, Z. Yuan, X. Huang, K. Jin, S. Yang and Y. Li, *J. Chem. Technol. Biotechnol.*, 2023, **98**, 1222–1237.
45 Y. Gu, X. Li, G. Ye, Z. Gao, W. Xu and Y. Sun, *New J. Chem.*, 2021, **45**, 9591–9597.
46 K. Li, X. An, K. H. Park, M. Khraisheh and J. Tang, *Catal. Today*, 2014, **224**, 3–12.
47 K. H. Do, D. Praveen Kumar, A. Putta Rangappa, J. Wang, Y. Hong, E. Kim, D. Amaranatha Reddy and T. Kyu Kim, *Mater. Today Chem.*, 2021, **22**, 100589.
48 R. Du, K. Xiao, B. Li, X. Han, C. Zhang, X. Wang, Y. Zuo, P. Guardia, J. Li, J. Chen, J. Arbiol and A. Cabot, *Chem. Eng. J.*, 2022, **441**, 135999.
49 Y. Wu, H. Ji, Q. Liu, Z. Sun, P. Li, P. Ding, M. Guo, X. Yi, W. Xu, C.-C. Wang, S. Gao, Q. Wang, W. Liu and S. Chen, *J. Hazard. Mater.*, 2022, **424**, 127563.
50 W. Jiang, H. Loh, B. Q. L. Low, H. Zhu, J. Low, J. Z. X. Heng, K. Y. Tang, Z. Li, X. J. Loh, E. Ye and Y. Xiong, *Appl. Catal., B*, 2023, **321**, 122079.
51 J. H. Cavka, S. Jakobsen, U. Olsbye, N. Guillou, C. Lamberti, S. Bordiga and K. P. Lillerud, *J. Am. Chem. Soc.*, 2008, **130**, 13850–13851.
52 L. Valenzano, B. Civalleri, S. Chavan, S. Bordiga, M. H. Nilsen, S. Jakobsen, K. P. Lillerud and C. Lamberti, *Chem. Mater.*, 2011, **23**, 1700–1718.
53 Q. Yu, Y. Zhou and C. Gao, *Desalination*, 2024, 117917.
54 R. R. Solís, M. Peñas-Garzón, C. Belver, J. J. Rodriguez and J. Bedia, *J. Environ. Chem. Eng.*, 2022, **10**, 107122.
55 T. Zhang, J.-Z. Wei, X.-J. Sun, X.-J. Zhao, H. Tang, H. Yan and F.-M. Zhang, *Inorg. Chem. Commun.*, 2020, **111**, 107671.
56 K. Gayathri, K. Vinothkumar, Y. N. Teja, B. M. Al-Shehri, M. Selvaraj, M. Sakar and R. G. Balakrishna, *Colloids Surf., A*, 2022, **653**, 129992.
57 Q. Su, J. Li, B. Wang, Y. Li and L. Hou, *Appl. Catal., B*, 2022, **318**, 121820.
58 D. N. G. Krishna and J. Philip, *Appl. Surf. Sci. Adv.*, 2022, **12**, 100332.
59 J. Wang, Z. Wang, K. Dai and J. Zhang, *J. Mater. Sci. Technol.*, 2023, **165**, 187–218.
60 X. Sun, J. Liu, H. Wang, Q. Li, J. Zhou, P. Li, K. Hu, C. Wang and B. Jiang, *Chem. Eng. J.*, 2023, **472**, 144750.
61 J. Liu, X. Huang, L. Hu, P. Liu, L. Jia, K. Sasaki, Z. Tan and H. Yu, *Chem. Eng. J.*, 2023, **476**, 146768.
62 X. Yang, T. Wang, H. Ma, W. Shi, Z. Xia, Q. Yang, P. Zhang, R. Ma, G. Xie and S. Chen, *J. Mater. Sci. Technol.*, 2024, **182**, 210–219.
63 S. Ren, J. Dong, X. Duan, T. Cao, H. Yu, Y. Lu and D. Zhou, *Chem. Eng. J.*, 2023, **460**, 141884.
64 A. Meng, B. Zhu, Y. Zhong, S. Zhou, P. Han and Y. Su, *Energy Rev.*, 2023, **2**, 100052.
65 P. Hu, R. Wang, Z. Gao, S. Jiang, Z. Zhao, H. Ji and Z. Zhao, *Appl. Catal., B*, 2021, **296**, 120371.
66 R. Ji, Z. Zhang, L. Tian, L. Jin, Q. Xu and J. Lu, *Chem. Eng. J.*, 2023, **453**, 139897.
67 T. Li, N. Tsubaki and Z. Jin, *J. Mater. Sci. Technol.*, 2024, **169**, 82–104.
68 J. Cai, B. Liu, S. Zhang, L. Wang, Z. Wu, J. Zhang and B. Cheng, *J. Mater. Sci. Technol.*, 2024, **197**, 183–193.
69 N. Li, Y.-L. Ma, H.-J. Zhang, D.-Y. Zhou, B.-L. Yao, J.-F. Wu, X.-P. Zhai, B. Ma, M.-J. Xiao, Q. Wang and H.-L. Zhang, *Mater. Today Chem.*, 2024, **41**, 102306.
70 Z. Li, J. Zi, X. Luan, Y. Zhong, M. Qu, Y. Wang and Z. Lian, *Adv. Funct. Mater.*, 2023, **33**, 2303069.
71 X. Chen, Y. Cai, R. Liang, Y. Tao, W. Wang, J. Zhao, X. Chen, H. Li and D. Zhang, *Appl. Catal., B*, 2020, **267**, 118687.
72 Z. Barbieriková, D. Dvoranová and V. Brezová, in *Materials Science in Photocatalysis*, ed. E. I. García-López and L. Palmisano, Elsevier, 2021, pp. 125–138.
73 X. Meng, G. Peng, Y. Yan, X. Wang, J. Zhu, C. Belver, W. Gong and L. Blaney, *Sep. Purif. Technol.*, 2025, **354**, 128502.
74 N. Yuan, Y. Mei, Y. Liu, Y. Xie, B. Lin and Y. Zhou, *J. CO_2 Util.*, 2022, **64**, 102151.
75 Z. Zeng, Z. Deng, T. Wang, H. Huang and Y. Guo, *Sep. Purif. Technol.*, 2023, **311**, 123264.
76 A. H. Bashal, K. Alkanad, M. Al-Ghorbani, S. Ben Aoun and M. A. Bajiri, *J. Environ. Chem. Eng.*, 2023, **11**, 109545.
77 K. Wang, T. Sun, H. Ma, Y. Wang, Z.-H. He, H. Wang, W. Wang, Y. Yang, L. Wang and Z.-T. Liu, *Chem. Eng. J.*, 2024, **497**, 154711.
78 H. Liu, Y. Yang, C. Guo and Y. Zhou, *Catal. Sci. Technol.*, 2024, **14**, 5938–5948.
79 Y. A. Alli, P. O. Oladoye, A. T. Onawole, H. Anuar, S. Adewuyi, O. D. Ogunbiyi and K. Philippot, *Fuel*, 2023, **344**, 128101.
80 S. Xiao, Y. Guan, H. Shang, H. Li, Z. Tian, S. Liu, W. Chen and J. Yang, *J. CO_2 Util.*, 2022, **55**, 101806.
81 J. Sun, Y. Guan, G. Yang, S. Qiu, H. Shao, Y. Wang, G. Li and S. Xiao, *ACS Sustain. Chem. Eng.*, 2023, **11**, 14827–14840.
82 Z. Yang, X. Tong, J. Feng, S. He, M. Fu, X. Niu, T. Zhang, H. Liang, A. Ding and X. Feng, *Chemosphere*, 2019, **220**, 98–106.
83 K. Wang, J. Wu, M. Zhu, Y.-Z. Zheng and X. Tao, *J. Solid State Chem.*, 2020, **284**, 121200.
84 F. Mu, Q. Cai, H. Hu, J. Wang, Y. Wang, S. Zhou and Y. Kong, *Chem. Eng. J.*, 2020, **384**, 123352.
85 Q. Li, Y. Shi, Z. Wang, C. Liu, J. Bi, J. C. Yu and L. Wu, *J. Colloid Interface Sci.*, 2023, **652**, 1568–1577.
86 Y. Gao, Y. Huang, M. Bao, X. Zhang, X. Zhou, L. Liu, Z. Zhang, L. Zeng and J. Ke, *Process Saf. Environ. Prot.*, 2023, **172**, 857–868.
87 P. Zhu, H. Cao, H. Yang, M. Geng, S. Qin, L. Tan, X. Gao and C. Wang, *Appl. Surf. Sci.*, 2024, **652**, 159348.
88 H. Guo, L. Luan, J. Cai, X. Ji, H. Yu and Y. Huang, *Chem. Eng. J.*, 2024, **479**, 147720.

89 M. Cabrero-Antonino, A. Melillo, E. Montero-Lanzuela, M. Álvaro, B. Ferrer, I. Vayá, H. G. Baldoví and S. Navalón, *Chem. Eng. J.*, 2023, **468**, 143553.
90 X. Feng, H. S. Jena, C. Krishnaraj, K. Leus, G. Wang, H. Chen, C. Jia and P. Van Der Voort, *ACS Appl. Mater. Interfaces*, 2021, **13**, 60715–60735.
91 Y. He, C. Li, X.-B. Chen, Z. Shi and S. Feng, *ACS Appl. Mater. Interfaces*, 2022, **14**, 28977–28984.
92 S.-Q. Wang, X. Gu, X. Wang, X.-Y. Zhang, X.-Y. Dao, X.-M. Cheng, J. Ma and W.-Y. Sun, *Chem. Eng. J.*, 2022, **429**, 132157.
93 X. Su, T. Xu, R. Ye, C. Guo, S. M. Wabaidur, D.-L. Chen, S. Aftab, Y. Zhong and Y. Hu, *J. Colloid Interface Sci.*, 2023, **646**, 129–140.
94 Y. Xie, N. Yuan, H. Liu, L. Luo, J. Gong, X. Yin, T. Li and Y. Zhou, *Appl. Catal., A*, 2024, **674**, 119616.
95 S. Hussain, Y. Wang, L. Guo and T. He, *J. Photochem. Photobiol., C*, 2022, **52**, 100538.
96 S. Yang, W. J. Byun, F. Zhao, D. Chen, J. Mao, W. Zhang, J. Peng, C. Liu, Y. Pan, J. Hu, J. Zhu, X. Zheng, H. Fu, M. Yuan, H. Chen, R. Li, M. Zhou, W. Che, J.-B. Baek, J. S. Lee and J. Xu, *Adv. Mater.*, 2024, **36**, 2312616.
97 X. Wang, G. Yang, G. Chai, M. S. Nasir, S. Wang, X. Zheng, C. Wang and W. Yan, *Int. J. Hydrogen Energy*, 2020, **45**, 30634–30646.
98 X. Wang, Y. Su, G. Yang, G. Chai, Z. Xu, M. S. Nasir, X. Zheng, C. Wang and W. Yan, *Int. J. Hydrogen Energy*, 2021, **46**, 11621–11635.
99 X. Zhao, M. Xu, X. Song, W. Zhou, X. Liu, Y. Yan and P. Huo, *Chem. Eng. J.*, 2022, **437**, 135210.
100 S. Dharani, S. Vadivel, L. Gnanasekaran and S. Rajendran, *Fuel*, 2023, **349**, 128688.
101 S. Qiao, M. Di, J.-X. Jiang and B.-H. Han, *EnergyChem*, 2022, **4**, 100094.
102 S. R. Firoozabadi, M. R. Khosravi-Nikou and A. Shariati, *J. Environ. Chem. Eng.*, 2023, **11**, 110978.
103 Y. Xue, M. Kamali, X. Zhang, N. Askari, C. De Preter, L. Appels and R. Dewil, *Environ. Pollut.*, 2023, **316**, 120549.
104 S. Li, W. Xu, L. Meng, W. Tian and L. Li, *Small Sci.*, 2022, **2**, 2100112.
105 N. Liu, B. Hu, K. Tang, T. Xia, F. Li, G. Quan, X. Zhang and L. Tang, *Surf. Interfaces*, 2023, **41**, 103134.
106 L. Hong, R. Guo, Z. Zhang, Y. Yuan, X. Ji, Z. Lin and W. Pan, *J. CO_2 Util.*, 2021, **51**, 101650.
107 W. Wang, S. Song, P. Wang, M. He, Z. Fang, X. Yuan, H. Li, C. Li, X. Wang, Y. Wei, W. Song, H. Xu and Z. Li, *ACS Catal.*, 2023, **13**, 4597–4610.
108 D. Li, B. Zhu, Z. Sun, Q. Liu, L. Wang and H. Tang, *Front. Chem.*, 2021, **9**, 804204.
109 N. Kong, H. Du, Z. Li, T. Lu, S. Xia, Z. Tang and S. Song, *Colloids Surf., A*, 2023, **663**, 131005.
110 X. Zhao, L. Sun, X. Jin, M. Xu, S. Yin, J. Li, X. Li, D. Shen, Y. Yan and P. Huo, *Appl. Surf. Sci.*, 2021, **545**, 148967.
111 M. Zhang, X. Wang, X. Qi, H. Guo, L. Liu, Q. Zhao and W. Cui, *J. Catal.*, 2022, **413**, 31–47.
112 W. Xiong, W. Ouyang, M. Li, H. Song, C. Zhao, M. Hu, S. Bai, Y. Liu, Y. Wu, Y. Zhang, Y. Liu and A. Pan, *Appl. Surf. Sci.*, 2024, **644**, 158807.
113 T.-A. Quach, V. N. Gopalakrishnan, J. Becerra, D.-T. Nguyen, J. M. E. Ahad, S. Mohan and T.-O. Do, *Catal. Today*, 2023, **421**, 114218.
114 S. Li, H. Li, Y. Wang, Q. Liang, M. Zhou, D. Guo and Z. Li, *Sep. Purif. Technol.*, 2024, **333**, 125994.
115 Y. Yuan, R. Guo, L. Hong, X. Ji, Z. Lin, Z. Li and W. Pan, *Mater. Today Energy*, 2021, **21**, 100829.
116 J. Sharma, P. Dhiman, A. Kumar and G. Sharma, *Environ. Res.*, 2024, **240**, 117431.
117 H. Guo, T. Zhang, W. Ma, S. Cheng, J. Ding, Q. Zhong and S. Kawi, *Fuel*, 2023, **344**, 127911.
118 Y. Mei, N. Yuan, Y. Xie, Y. Li, B. Lin and Y. Zhou, *Appl. Surf. Sci.*, 2022, **597**, 153725.
119 J. Li, H. Yuan, W. Zhang, B. Jin, Q. Feng, J. Huang and Z. Jiao, *Carbon Energy*, 2022, **4**, 294–331.
120 J. Fu, Q. Xu, J. Low, C. Jiang and J. Yu, *Appl. Catal., B*, 2019, **243**, 556–565.
121 F. Li, G. Zhu, J. Jiang, L. Yang, F. Deng, Arramel and X. Li, *J. Mater. Sci. Technol.*, 2024, **177**, 142–180.
122 P. Hao, Z. Chen, Y. Yan, W. Shi and F. Guo, *Sep. Purif. Technol.*, 2024, **330**, 125302.
123 B. Qiao, A. Wang, X. Yang, L. F. Allard, Z. Jiang, Y. Cui, J. Liu, J. Li and T. Zhang, *Nat. Chem.*, 2011, **3**, 634–641.
124 C. Gao, J. Low, R. Long, T. Kong, J. Zhu and Y. Xiong, *Chem. Rev.*, 2020, **120**, 12175–12216.
125 G. Wang, C.-T. He, R. Huang, J. Mao, D. Wang and Y. Li, *J. Am. Chem. Soc.*, 2020, **142**, 19339–19345.
126 M. Chu, Y. Li, X. Chen, G. Hou, Y. Zhou, H. Kang, W. Qin and X. Wu, *J. Mater. Chem. A*, 2022, **10**, 23666–23674.
127 T.-A. Quach, M.-K. Duong, S. Mohan and T.-O. Do, *ACS Appl. Energy Mater.*, 2024, **7**, 8797–8806.
128 C. Yu, X. Zhang, C. Song, Y. Wang, J. Lin, Z. Guo, Y. Zhang, Z. Liu, C. Li, Y. Sun, C. Tang and Y. Huang, *Chem. Eng. J.*, 2024, **499**, 156088.
129 M. Duflot, C. Marchal, V. Caps, V. Artero, K. Christoforidis and V. Keller, *Catal. Today*, 2023, **413–415**, 114018.
130 W. Huang, Z. Zhang, J. Xu, H. Cui, K. Tang, D. Crawshaw, J. Wu, X. Zhang, L. Tang and N. Liu, *JACS Au*, 2025, **5**(3), 1184–1195.
131 X. Liu, C. Zhu, M. Li, H. Xing, S. Zhu, X. Liu and G. Zhu, *Angew. Chem., Int. Ed.*, 2024, **63**, e202412408.
132 H. Yu, S. Guo, M. Jia, J. Jia, Y. Chang and J. Wang, *Arabian J. Chem.*, 2024, **17**, 105975.
133 R. Wang, W. Cheng, H. Wang, Q. Mei, X. Li, B. Bai and Q. Wang, *J. Environ. Chem. Eng.*, 2025, **13**, 115360.
134 X. Li, C. Fang, L. Huang and J. Yu, *J. Colloid Interface Sci.*, 2024, **655**, 485–492.
135 X. Ma, Y. Zhang, A. Zhou, Y. Jia, Z. Xie, L. Ding and J.-R. Li, *J. Colloid Interface Sci.*, 2025, **685**, 696–705.
136 H.-N. Wang, Y.-H. Zou, Y.-M. Fu, X. Meng, L. Xue, H.-X. Sun and Z.-M. Su, *Nanoscale*, 2021, **13**, 16977–16985.
137 X. Wang, Y. Liu, G. Chai, G. Yang, C. Wang and W. Yan, *Chem.–Eur. J.*, 2022, **28**, e202200583.

138 S. Ali, A. Razzaq, H. Kim and S.-I. In, *Chem. Eng. J.*, 2022, **429**, 131579.
139 C. B. Hiragond, N. S. Powar, J. Lee and S.-I. In, *Small*, 2022, **18**, 2201428.
140 L. Liao, G. Xie, X. Xie and N. Zhang, *J. Phys. Chem. C*, 2023, **127**, 2766–2781.
141 S. R. Wenger, E. R. Kearns, K. L. Miller and D. M. D'Alessandro, *ACS Appl. Energy Mater.*, 2023, **6**, 9074–9083.
142 Y. Wang, Q. Yang, F. Yi, R. Lu, Y. Chen, C. Liu, X. Li, C. Wang and H. Yan, *ACS Appl. Mater. Interfaces*, 2021, **13**, 29916–29925.
143 J. Chen, Y. Yang, S. Zhao, F. Bi, L. Song, N. Liu, J. Xu, Y. Wang and X. Zhang, *ACS Catal.*, 2022, **12**, 8069–8081.
144 M. Ali, E. Pervaiz and O. Rabi, *ACS Omega*, 2021, **6**, 34219–34228.